



## Scaling rockburst hazard using the DDA and GSI methods



Yossef H. Hatzor<sup>a,\*</sup>, Ben-Guo He<sup>a</sup>, Xia-Ting Feng<sup>b</sup>

<sup>a</sup> Department of Geological and Environmental Sciences, Ben-Gurion University of the Negev, Beer Sheva 84105, Israel

<sup>b</sup> State Key Laboratory of Geomechanics and Geotechnical Engineering, Institute of Rock and Soil Mechanics, Chinese Academy of Sciences, Wuhan 430071, China

### ARTICLE INFO

#### Keywords:

Tunneling  
Rockbursts  
GSI  
DDA

### ABSTRACT

We examine the influence of rock mass quality, as scaled by the Geological Strength Index (GSI), on energy redistribution in tunnels driven through discontinuous rock masses. We assume that in blocky rock masses rockbursts develop as abrupt motion of finite rigid blocks along pre-existing discontinuities rather than by fracture of intact rock elements. We begin by formulating analytically the local energy density around a tunnel in continuous, homogenous, isotropic, linear-elastic medium and demonstrate the significance of the initial principal stress ratio on the result. We then introduce discontinuities into the rock mass and find analytically the peak acceleration of an ejected keyblock when it flies into the tunnel space, to demonstrate the viability of this mechanism as a potential rockbursting source. Using the numerical discontinuous deformation analysis (DDA) method we find the total kinetic energy released during rockbursting and validate our DDA results using monitored seismic energy emissions detected during an intensive rockburst event encountered while excavating one of the headrace tunnels at Jinping II hydroelectric project in China. Utilizing an analytical solution we published earlier for the redistribution of energy components due to tunneling, we explore the effect of rock mass quality as scaled by GSI on the elastic strain energy, dissipated energy, and kinetic energy. We find that the elastic strain energy and the energy dissipated by shear generally decrease with increasing GSI value. The kinetic energy of rockbursts however shows a more complicated behavior. It is low at low quality rock masses, peaks at GSI value of about 60, and decreases again with increasing rock mass quality. This result is supported by documented rockbursts during excavation of the deep tunnels of the Jinping II hydropower project, where the majority of rockbursts were recorded in tunnel segments with characteristic GSI values between 60 and 75.

### 1. Introduction

Rockbursts are the most serious and least understood hazard associated with deep underground excavations, typically involving violent energy release with sudden ejection of rock fragments that may result in fatalities and damage to facilities (Mazaira and Konicek, 2015). Not unlike artificially induced earthquakes (Zembaty, 2004) triggered by changes in the stress field near the excavation, rock bursts are accompanied by audible acoustic emissions, and trigger ground motions strong enough to eject preexisting rock blocks into the excavation space. Excavation-induced stress concentrations at great depths further increase the risk for spontaneous rockbursts.

With the increase in attempted underground excavation depths, the risk for uncontrolled rockbursts has increased as well. Our ability to predict the temporal and spatial distribution of rockbursts, as well as their magnitudes, however, is constrained by our theoretical understanding of this phenomenon. A fundamental contribution to this field led by the late Professor Neville Cook has been made in South Africa

during the 1960's (Cook, 1966). Since then, several research groups from around the world have attempted to explore this issue and to offer efficient prevention measures (Kaiser and Cai, 2012). Based on field observations three rock burst types have been discussed: (1) strain bursts, (2) pillar bursts, and (3) fault slip bursts (Müller, 1991), among which strain bursts are most frequently encountered underground (He et al., 2015). To date, two causative mechanisms have been suggested for triggering rockbursts: (1) remote seismic events, and (2) stress changes close to the excavation boundaries (Ortlepp and Stacey, 1994). It is widely accepted however that stress changes near the excavation boundaries are more significant than remote seismic events (Wang et al., 2015a,b). Rockburst damage intensity is typically discussed in terms of the depth of rockburst notches, volume of rock failed, and seismic energy released. Recently the concept of excavation damage zone (EDZ) around underground openings has been employed in brittle rock masses to predict the depth and extent of rock fracturing as a result of rockbursts (Perras and Diederichs, 2016).

Different rockburst intensity classifications have been developed

\* Corresponding author.

E-mail address: [hatzor@bgu.ac.il](mailto:hatzor@bgu.ac.il) (Y.H. Hatzor).

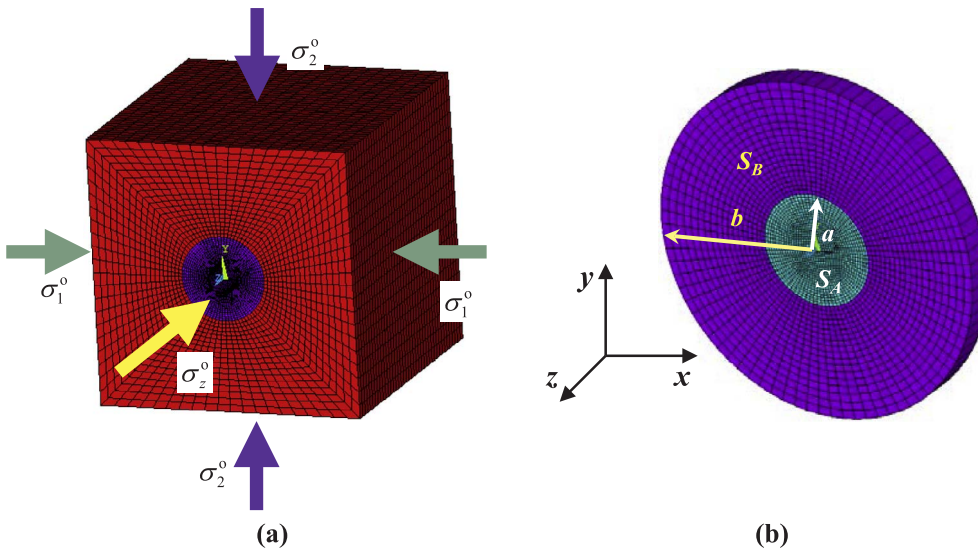


Fig. 1. Sign convention used in this paper: (a) assumed initial stress state; (b) the excavated tunnel of radius  $a$  and the analyzed annulus of radius  $b$ .

based on experience from different countries (Martin, 1970). The diversity in approaches is evident in the multitude of stress-based criteria. Four well-known such criteria are the ratio between uniaxial compressive strength and the vertical *in-situ* stress (Hoek and Brown, 1980), the sum of the tangential stress and the horizontal stress parallel to the tunnel axis ( $\sigma_\theta + \sigma_L$ ) (Turchaninov et al., 1972), the magnitude of the major principal stress  $\sigma_1$  (Barton et al., 1974), and the magnitude of the tangential stress  $\sigma_\theta$  (Russenes, 1974). Analyzing a single rockburst event with these different criteria yields, however, inconsistencies in the rockburst intensity classification (Zhao et al., 2017). Moreover, none of these criteria includes the influence of the excavation dimension on rockburst potential.

Geophysical methods have been utilized to detect the evolution of mining-induced tremors, both in time and in space, and the results have been used to study fracture initiation and propagation and to assess the corresponding energy accumulation and release (e.g., Brady and Leighton (1977)). Three-dimensional monitoring of micro-seismic (MS) tremors now provides powerful means to detect the location of and compute the seismic energy released from mining-induced motions (Feng et al., 2012). Assessment of rockburst hazard based on recorded seismicity is now standard engineering practice, assisting in making operational decisions in the course of the deep excavation projects, on a daily basis (Mutke et al., 2015). It is recognized however that the phenomenon of rock bursts involves both static as well as dynamic deformation (Adoko et al., 2013).

At the laboratory, true-triaxial unloading experiments have been conducted to clarify the relationship between rockbursts and acoustic emissions in the process of fracturing of prismatic limestone specimens (Gong et al., 2014). Instantaneous rockbursts in granites were studied at the lab to understand the relative distribution of energy components, i.e., the total, elastic, and dissipated energy for a single rock block (Wang et al., 2015a,b). To investigate the mechanisms of rock bursts caused by shear failure along pre-existing interfaces, model experiments and direct shear tests were performed (Zhou et al., 2015).

Numerical methods are useful for assessing the potential for rock bursts and for modeling prevention measures. Based on numerical analysis several indices have been suggested, e.g., failure approach indices which evaluate the stress concentration in the rock mass using a “yield approach index” or a “failure degree index” (Zhang et al., 2011). Three-dimensional finite element modeling was conducted to study stress concentrations after the opening is created in deep, hard rock mines (Wang and Park, 2001). The explicit finite difference FLAC code also was used to compute and analyze the distribution and accumulation of elastic strain energy in the rock mass that was treated as a

continuum during an unloading opening (Miao et al., 2016). In combination with experimental results and continuum-based modeling, the strain energy stored in the rock was studied, and rockburst occurrence was assessed using evaluation indices like energy release rate (ERR), energy storage rate (ESR) (Cook, 1966), burst potential index (BPI), and potential energy of elastic strain (PES).

When using continuum based numerical approaches that employ infinitesimal strain theory, separation, rotation, or ejection of finite rock blocks cannot be modeled rigorously. This restriction may be relaxed by using discrete element approaches such as the numerical explicit DEM or the implicit DDA methods.

A useful way to describe the structure of the rock mass is by means of empirical rock mass classification methods that address geometrical attributes like joint set attitude and mean joint set spacing. These geometrical parameters control the block size distribution in the rock mass. Intuitively, it would be expected that the energy associated with rockbursts would be strongly influenced by the blocky structure of the rock mass, however to date this issue has not been studied thoroughly enough. We explore here the relationship between rock mass quality, as scaled by the Geological Strength Index (GSI), and the redistribution of energy components due to tunneling, with particular emphasis on the kinetic energy of keyblock ejections, or rockbursts in the context of this paper.

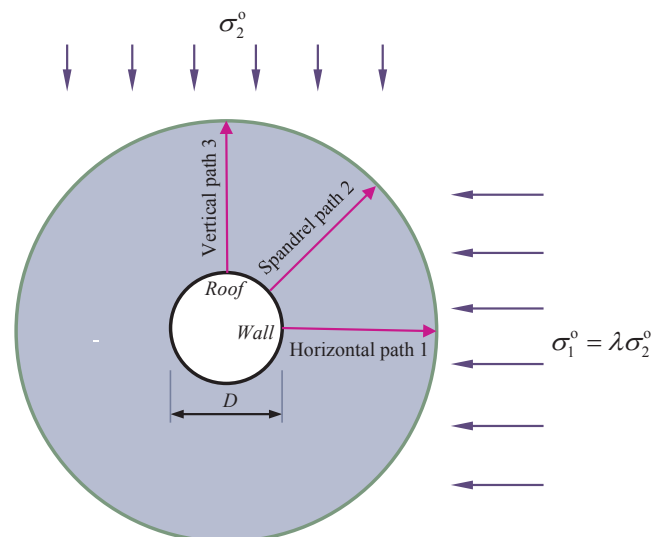


Fig. 2. Three radial paths considered in the analysis.

We assume in this paper that in an initially discontinuous rock mass the rockburst phenomena will be dominated by ejection of pre-existing rock blocks rather than by induced fracture in initially intact rock elements. We base our analysis on a theoretical derivation of the energy density redistribution once the tunnel is formed in a linear elastic continuum, and thus define the “affected zone” due to tunneling. We then introduce discontinuities within the affected zone of varying spacing, orientation, and frictional resistance so as to model rock mass qualities ranging between GSI = 50–80. With increasing rock mass quality, the Young’s modulus of intact rock elements, the characteristic block size, and joint friction all increase, whereas the number of joint sets in the rock mass decreases. We find that while the elastic strain energy stored in the rock mass and the dissipated energy by shear sliding decreases with increasing GSI, the kinetic energy associated with ejected rock blocks, or rockbursts in our context, peaks at GSI values near 60.

2. Theoretical considerations

2.1. Redistribution of strain energy

The strain energy stored in the rock mass determines the amount of energy available for generating rockbursts once the opening is made. Rockburst potential will increase, therefore, with increasing stored energy (Obert and Duvall, 1967). To determine the elastic strain energy stored in the rock we employ Kirsch solution (Kirsch, 1898) for a semi-infinite underground space subjected to initial principal far field stresses under plane strain conditions (see Fig. 1). In the notation adopted here “pre” and “post” excavation states are designated by superscripts (\*) and

(\*), respectively; for the general case no superscript is used.

The initial strain energy  $U_{A,B}^0$  stored in  $S_A$  and  $S_B$  (refer to Fig. 1) can be expressed using Eq. (1) (for complete derivation see He et al. (2016)), where  $E$  is Young’s modulus,  $\nu$  is Poisson’s ratio, and  $\sigma_1^0, \sigma_2^0$  are the initial principal stresses:

$$U_{A,B}^0 = \frac{1}{2E} [(1-\nu^2)(\sigma_1^0 + \sigma_2^0)^2 - 2(\nu + 1)\sigma_1^0\sigma_2^0] \times S_{A,B} \tag{1}$$

Once the tunnel is created, the stress concentrations in the proximity of the circular opening can be written in polar coordinates (Kirsch, 1898):

$$\begin{cases} \sigma_r^* = \frac{\sigma_1^0 + \sigma_2^0}{2} \left(1 - \frac{a^2}{r^2}\right) + \frac{\sigma_1^0 - \sigma_2^0}{2} \left(1 - \frac{a^2}{r^2}\right) \left(1 - \frac{3a^2}{r^2}\right) \cos 2\theta \\ \sigma_\theta^* = \frac{\sigma_1^0 + \sigma_2^0}{2} \left(1 + \frac{a^2}{r^2}\right) - \frac{\sigma_1^0 - \sigma_2^0}{2} \left(1 + \frac{3a^4}{r^4}\right) \cos 2\theta \\ \tau_{r\theta}^* = -\frac{\sigma_1^0 - \sigma_2^0}{2} \left(1 - \frac{a^2}{r^2}\right) \left(1 + \frac{3a^2}{r^2}\right) \sin 2\theta \end{cases} \tag{2}$$

Assuming linear elasticity, Hook’s law for this case can be written as (Timoshenko and Goodier, 1970):

$$\begin{cases} \epsilon_x = \frac{1}{E} [\sigma_x - \nu(\sigma_y + \sigma_z)] \\ \epsilon_y = \frac{1}{E} [\sigma_y - \nu(\sigma_x + \sigma_z)] \\ \epsilon_z = \frac{1}{E} [\sigma_z - \nu(\sigma_x + \sigma_y)] \\ \gamma_{xy} = \frac{2(1+\nu)}{E} \tau_{xy}, \quad \gamma_{yz} = \frac{2(1+\nu)}{E} \tau_{yz}, \quad \gamma_{zx} = \frac{2(1+\nu)}{E} \tau_{zx} \end{cases} \tag{3}$$

If the relation between each force and the corresponding displacement is linear, the elastic strain energy density per unit area is:

$$\phi = 1/2(\sigma_x \epsilon_x + \sigma_y \epsilon_y + \sigma_z \epsilon_z + \tau_{xy} \gamma_{xy} + \tau_{yz} \gamma_{yz} + \tau_{zx} \gamma_{zx}) \tag{4}$$

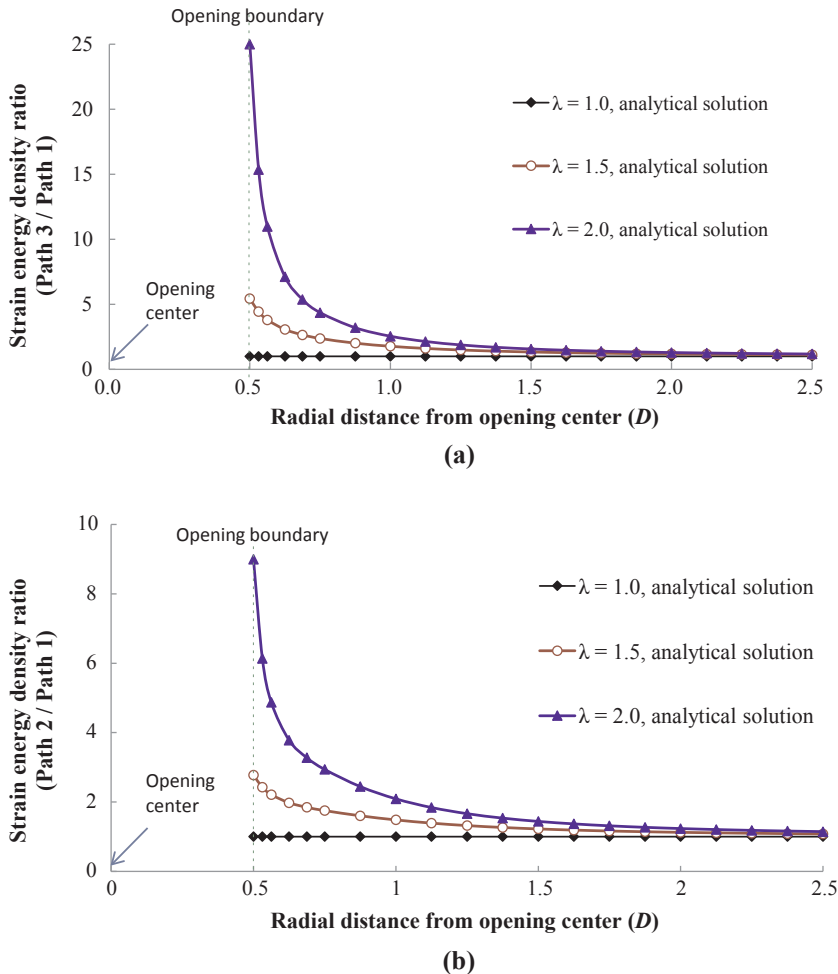


Fig. 3. Distribution of strain energy density concentration under various *in situ* principal stress ratios λ: (a) roof vs. sidewall (Path 3 / Path 1); (b) spandrel vs. sidewall (Path 2 / Path 1). Note that the energy density concentration is homogenous surrounding the opening under hydrostatic stress regime of λ = 1 for every r from tunnel center.

Substituting Eqs. (2) and (3) into Eq. (4) yields the excavation-induced strain energy density using local stress components after the excavation is made and assuming plane-strain conditions (for complete derivation see He et al. (2016)):

$$\phi^* = \frac{1 + \nu}{2E} [(1-\nu)(\sigma_x^* + \sigma_y^*)^2 - 2\sigma_x^* \sigma_y^* + 2\tau_{xy}^{*2}] \quad (5)$$

Using Eqs. (2) and (5) we can write specific expressions (for complete derivation see Appendix A) for the energy density distribution at the sidewall, spandrel, and roof of a circular opening of radius  $a$  at a radial distance  $r$  (see Fig. 2):

$$\begin{aligned} \phi_{\text{Sidewall}, \theta=0}^* &= \frac{1 + \nu}{2E} \left\{ (1-\nu) \left[ \sigma_1^0 + \sigma_2^0 - 2(\sigma_1^0 - \sigma_2^0) \frac{a^2}{r^2} \right]^2 \right. \\ &\quad - 2 \left( 1 - \frac{a^2}{r^2} \right) \left[ \frac{(\sigma_1^0 + \sigma_2^0)^2}{4} \left( 1 + \frac{a^2}{r^2} \right) - \frac{\sigma_1^0 - \sigma_2^0}{2} \frac{a^2}{r^2} \left( 1 + \frac{3a^2}{r^2} \right) \right. \\ &\quad \left. \left. - \frac{(\sigma_1^0 - \sigma_2^0)^2}{4} \left( 1 - \frac{3a^2}{r^2} \right) \left( 1 + \frac{3a^4}{r^4} \right) \right] \right\} \quad (6) \end{aligned}$$

$$\begin{aligned} \phi_{\text{Spandrel}, \theta=\frac{\pi}{4}}^* &= \frac{1 + \nu}{2E} \left[ (1-\nu)(\sigma_1^0 + \sigma_2^0)^2 - \frac{(\sigma_1^0 + \sigma_2^0)^2}{2} \left( 1 - \frac{a^4}{r^4} \right) \right. \\ &\quad \left. + \frac{(\sigma_1^0 - \sigma_2^0)^2}{2} \left( 1 - \frac{a^2}{r^2} \right)^2 \left( 1 + \frac{3a^2}{r^2} \right)^2 \right] \end{aligned}$$

$$\begin{aligned} \phi_{\text{Roof}, \theta=\frac{\pi}{2}}^* &= \frac{1 + \nu}{2E} \left\{ (1-\nu) \left[ \sigma_1^0 + \sigma_2^0 + 2(\sigma_1^0 - \sigma_2^0) \frac{a^2}{r^2} \right]^2 \right. \\ &\quad - 2 \left( 1 - \frac{a^2}{r^2} \right) \left[ \frac{(\sigma_1^0 + \sigma_2^0)^2}{4} \left( 1 + \frac{a^2}{r^2} \right) + \frac{\sigma_1^0 - \sigma_2^0}{2} \frac{a^2}{r^2} \left( 1 + \frac{3a^2}{r^2} \right) \right. \\ &\quad \left. \left. - \frac{(\sigma_1^0 - \sigma_2^0)^2}{4} \left( 1 - \frac{3a^2}{r^2} \right) \left( 1 + \frac{3a^4}{r^4} \right) \right] \right\} \end{aligned}$$

Strain energy density ratios for two paths in a rock mass with Young's modulus  $E = 25.3 \text{ GPa}$  and Poisson's ratio  $\nu = 0.22$  are plotted in Fig. 3. For initial principal stress ratio  $\lambda$  greater than 1.0, the energy density at the roof (Fig. 3a) is much higher than at the sidewall (Fig. 3b), as would be intuitively anticipated considering Kirsch solution, because the initial horizontal stress ( $\sigma_1^0 = \sigma_x^0$ ) is greater than the initial vertical stress ( $\sigma_2^0 = \sigma_y^0$ ). Generally, the energy density ratio increases with increasing  $\lambda$ . In underground environments where the *in situ* tectonic stresses are characterized by high stress ratios, therefore, rock bursts could indeed be triggered by induced fracture of intact rock elements in direction parallel to the opening surface (Obert and Duvall, 1967), at locations where the energy densities are at maximum. When the stress field is hydrostatic ( $\lambda = 1$ ), however, the energy density distribution is homogenous for every  $r$  around the opening, and therefore the potential for induced fracture of intact rock elements is equal all around the opening for any given  $r$ .

Inspection of the results plotted in Fig. 3 reveals that most of the increase in strain energy density is restricted to an annulus thickness of roughly half the tunnel diameter, from the opening boundary to a distance of one tunnel diameter ( $D$ ) from the tunnel center. At a distance greater than  $1.5D$  from the tunnel center the energy density increase appears to be negligible. This annulus, from  $0.5D$  to  $1.5D$  from tunnel center, has been referred to as the "Rockbursting Prone Zone" by He et al. (2016).

The total elastic strain energy can be obtained by integrating the

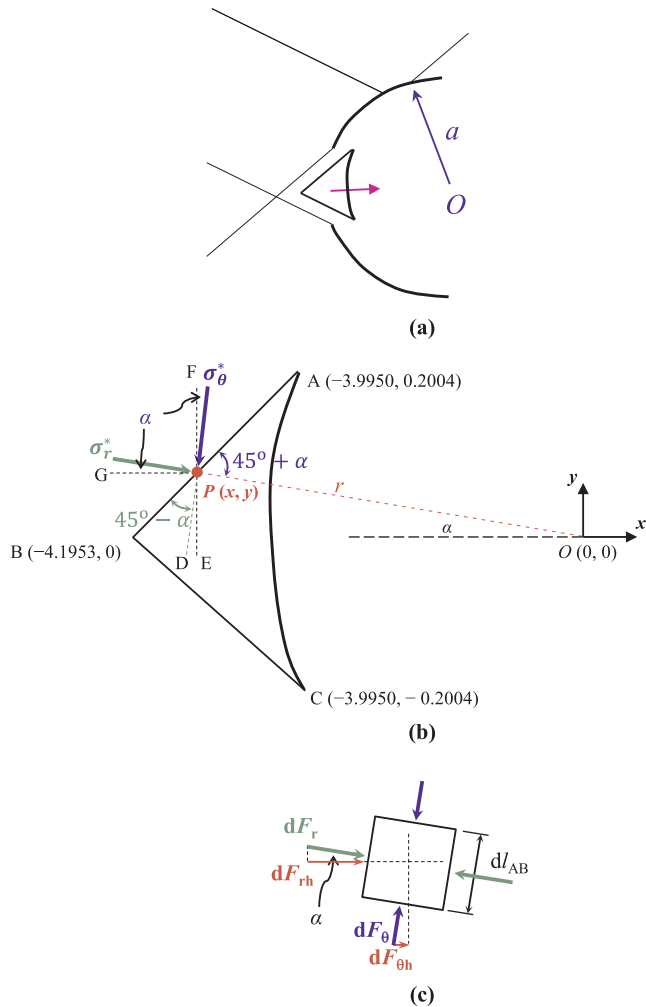


Fig. 4. Excavation-included keyblock ejection under initially hydrostatic stress: (a) schematic illustration of problem geometry and assumed keyblock flight trajectory; (b) principal stresses acting on upper block boundary in polar coordinates; (c) force equilibrium acting on an infinitesimal element.

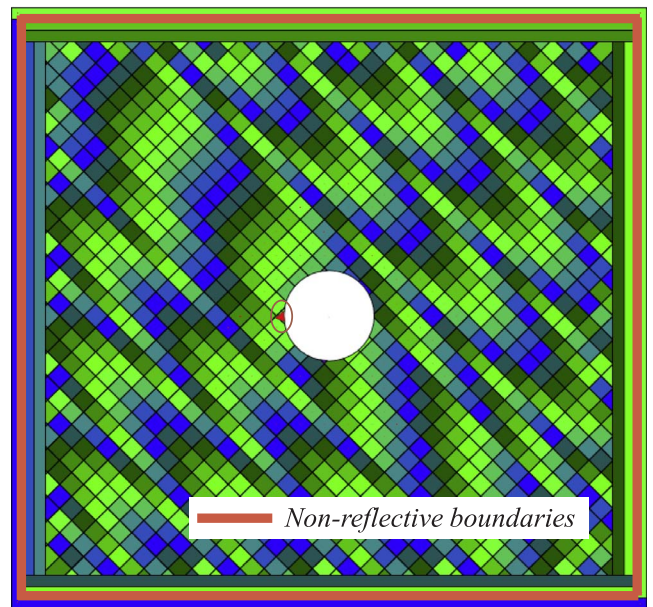


Fig. 5. DDA mesh used for DDA forward modeling utilizing sequence excavation (Tal et al., 2014) and non-reflective boundaries (Bao et al., 2012) enhancements. The candidate keyblock for excavation-induced ejection is marked.

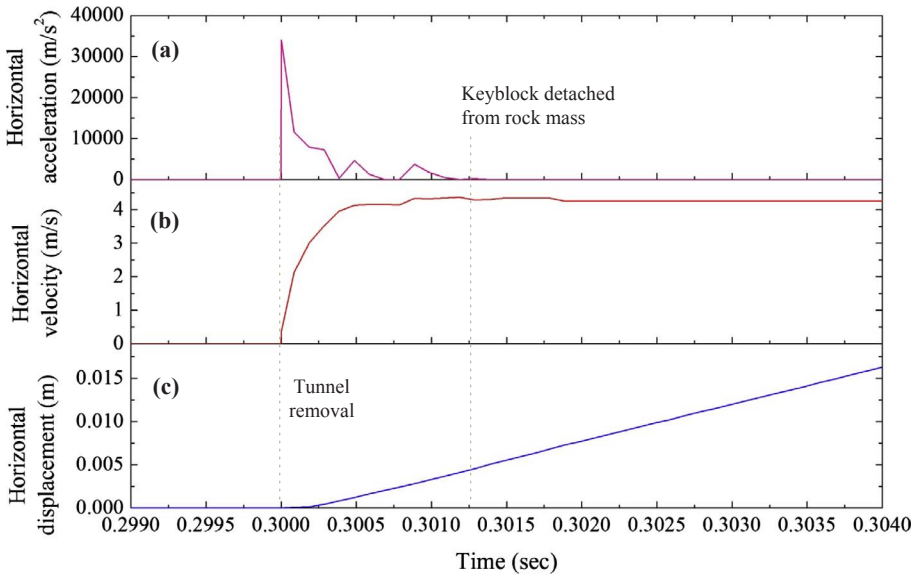


Fig. 6. Time histories of ejected keyblock once the opening is created under initial hydrostatic stress level of 30 MPa as obtained with DDA: (a) acceleration; (b) velocity; (c) displacement.

energy density  $\varphi^*$  (Eq. (5)) over area  $S_B$  as shown in Fig. 1b (for complete derivation see He et al. (2016)):

$$\begin{aligned}
 U_B^* &= \frac{\pi}{E} \left\{ (1-\nu^2) \int_a^b \left[ (\sigma_1^0 + \sigma_2^0)^2 r + 2(\sigma_1^0 - \sigma_2^0)^2 \frac{a^4}{r^3} \right] dr \right. \\
 &\quad \left. + 2(1+\nu) \int_a^b \left[ \frac{(\sigma_1^0 + \sigma_2^0)^2 a^4}{4r^3} + \frac{(\sigma_1^0 - \sigma_2^0)^2 a^4}{4} \left( \frac{2}{r^3} - \frac{12a^2}{r^5} + \frac{9a^4}{r^7} \right) - \sigma_1^0 \sigma_2^0 r dr \right] \right\} \\
 &= \frac{\pi}{E} \left\{ (1-\nu^2) \left[ \frac{1}{2} (\sigma_1^0 + \sigma_2^0)^2 r^2 \Big|_a^b - (\sigma_1^0 - \sigma_2^0)^2 a^4 \frac{1}{r^3} \Big|_a^b \right] \right. \\
 &\quad \left. + 2(1+\nu) \left[ -\frac{(\sigma_1^0 + \sigma_2^0)^2}{8} a^4 \frac{1}{r^2} \Big|_a^b + \frac{(\sigma_1^0 - \sigma_2^0)^2 a^4}{4} \left( -\frac{1}{r^2} \Big|_a^b + 3a^2 \frac{1}{r^4} \Big|_a^b - \frac{3}{2} a^4 \frac{1}{r^6} \Big|_a^b \right) \right. \right. \\
 &\quad \left. \left. - \frac{\sigma_1^0 \sigma_2^0}{2} r^2 \Big|_a^b \right] \right\} \tag{7}
 \end{aligned}$$

Eq. (7) can be used to calculate the magnitude of energy change due to the excavation in terms of the “Energy Increase Ratio”, defined as

$(U_B^* - U_B^0) / U_A^0$  for increasing distances from the tunnel center. He et al. (2016) showed that the energy increase ratio increases with distance until it reaches some constant value at infinity, the value of which is independent of initial stress ratio, initial stress magnitude, and/or opening size. Moreover, most of the energy increase occurs within an annulus that extends to a distance of  $3D$  from the tunnel center, beyond which the additional change in energy is negligible. He et al. (2016) termed the annulus between  $0.5D$  to  $3D$  the “affected zone”.

To study the influence of individual rock mass parameters on the energy redistribution we limit the analysis domain to the “Rockbursting Prone Zone”, as defined above. When studying the influence of rock mass quality on energy redistribution, however, we extend the analysis domain to the entire “affected zone”, to capture better the influence of the entire rock mass structure on energy redistribution following tunneling.

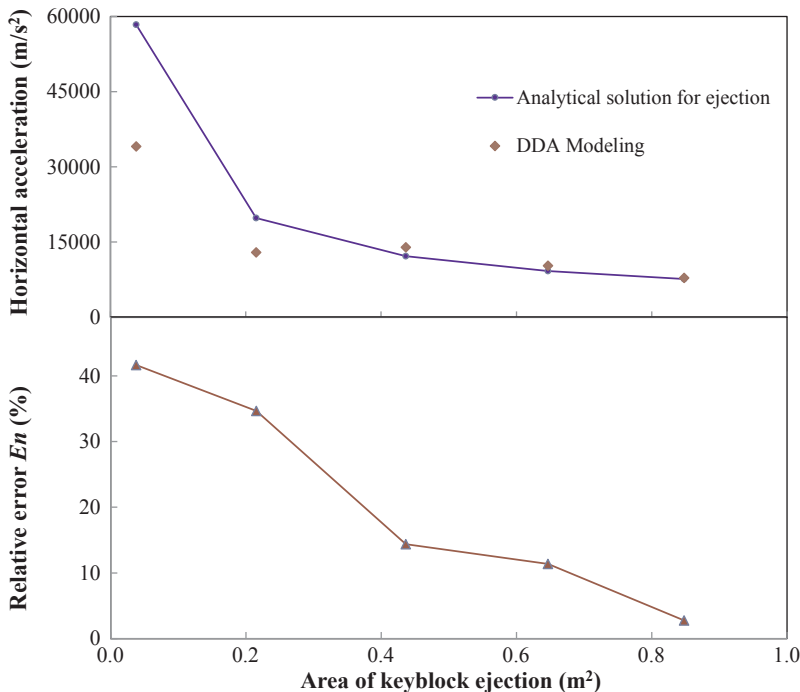


Fig. 7. DDA computation of peak horizontal acceleration of ejected keyblocks as a function of block size. The numerical error decreases from 41% for keyblock area of 0.038 m<sup>2</sup>, to 3% for block area of 0.85 m<sup>2</sup>.

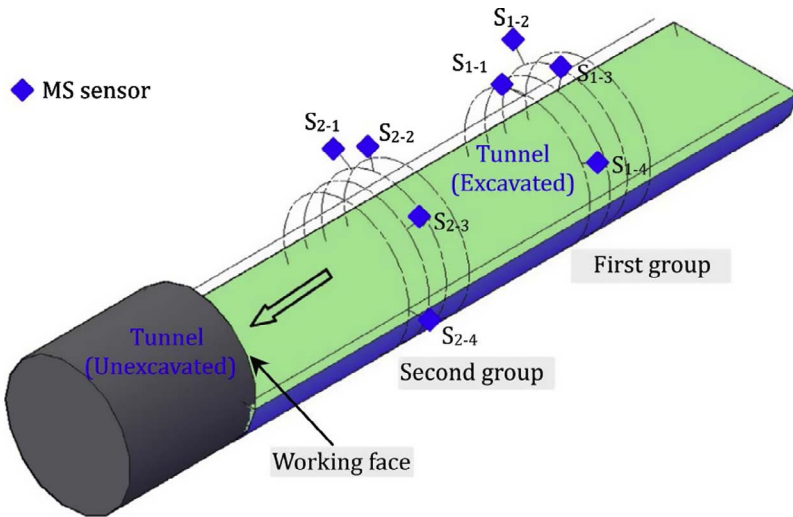


Fig. 8. Layout of micro-seismic sensor arrays used for monitoring seismic energy induced by rock bursts (modified after Chen et al. (2015)).

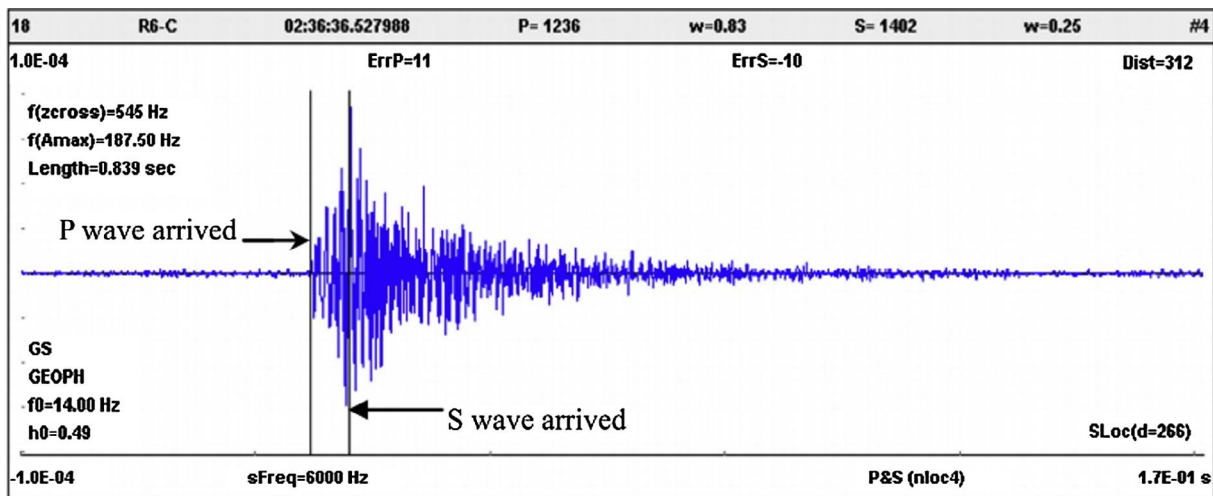


Fig. 9. Rockburst induced waveform as recorded by micro-seismic sensor array in Jinping II hydropower station (modified after Feng et al. (2016)).

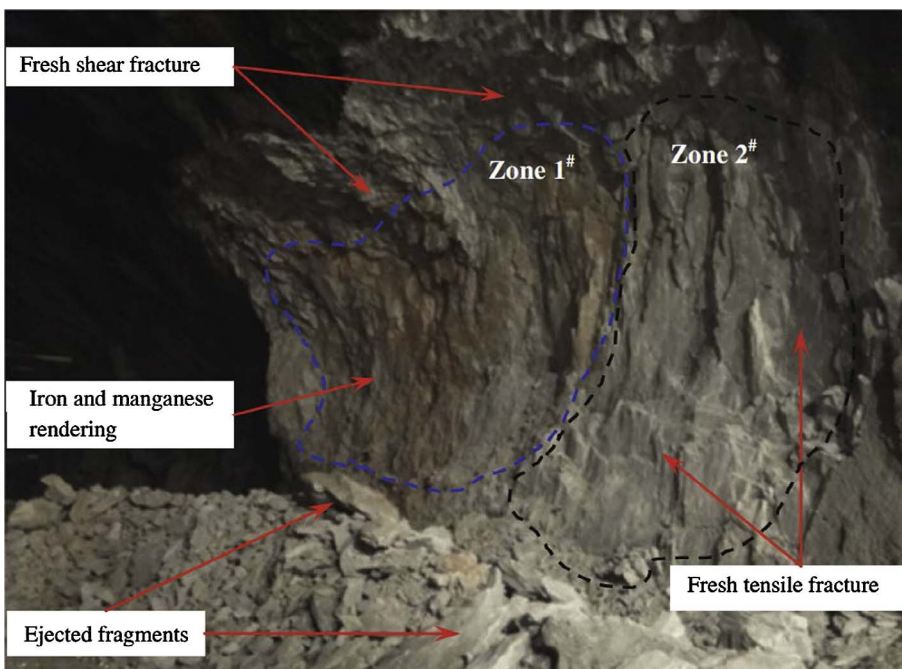


Fig. 10. A typical intensive rockburst at Stake K8 + 805–815 of No. 2 headrace tunnel at Jinping II hydropower Station (modified after Chen et al. (2015)).

2.2. Velocity of keyblock ejection

We have assumed a continuous rock mass in our theoretical discussion above. Real rock masses, however, are rarely continuous, with joints, faults, bedding and foliation planes typically transecting the rock mass. It is therefore imperative to study how the excavation-induced stress concentrations might affect the dynamic stability of an initially discontinuous rock mass. More specifically, are excavation-induced stress concentrations sufficiently high to trigger sudden block ejections from the surrounding rock once the underground space is formed? If this is so, rockbursts that arise from ejection of pre-existing, removable keyblocks (as defined by Goodman and Shi (1985)), must be considered in addition to rockbursts formed by fracturing of initially intact rock. In the theoretical analysis henceforth, we focus on rockbursts generated by ejection of keyblocks from the boundary of the tunnel into the newly created space.

We consider the force balance acting on a keyblock at the boundary of a circular excavation, formed by intersection of two orthogonal joints (see Fig. 4a). We assume the preexisting joints do not alter the initial stress distribution computed above for a continuous rock mass. If the frictional resistance is not sufficiently high, however, part of the stored elastic strain energy in the rock mass will be converted into kinetic energy of rockbursts once the underground space is formed.

Consider a keyblock bounded by two joints inclined symmetrically about the x-axis as shown in Fig. 4b, in a rock mass subjected to hydrostatic *in situ* stress. Because gravity is not considered, once the space is formed the keyblock shown in Fig. 4b will open from both boundary

joints without mobilizing any frictional resistance along traces  $l_{AB}$  or  $l_{BC}$ , and due to the symmetrical jointing pattern and the stress symmetry will fly in a horizontal trajectory into the newly formed space. Also due to symmetry, the horizontal force components acting on keyblock boundaries  $l_{AB}$  and  $l_{BC}$  must be equal. After integrating both the differentials  $dF_{rh}$  due to radial stress  $\sigma_r^*$  and  $dF_{\theta h}$  due to tangential stress  $\sigma_{\theta}^*$  (see Fig. 4c), we can find the peak acceleration of the keyblock at the instance it begins to move (for complete derivation see Appendix B):

$$a = \frac{F}{m} = \frac{2 \times (F_{rh} + F_{\theta h})}{S_{ejection} \times 1 \text{ m} \times \rho} = \frac{2 \times (1417365 \text{ N} + 1417419 \text{ N})}{0.038 \text{ m}^2 \times 1 \text{ m} \times 2563.8 \text{ kg/m}^3} = 58363 \text{ m/s}^2 \tag{8}$$

where the area of the keyblock is  $0.038 \text{ m}^2$  in this example (Fig. 4b).

Note that the analytically obtained peak keyblock acceleration under the imposed initial hydrostatic stress of 30 MPa is extremely high, in the order of  $5 \times 10^4 \text{ m/s}^2$ . The acceleration will immediately drop to zero, however, once the block is detached from the surrounding rock mass.

To see if this value is reasonable we employ the numerical, discrete-element, DDA method (Shi, 1993) with the exact same keyblock geometry and initial stresses as in the worked example. The input material properties are Young's modulus  $E = 20 \text{ GPa}$ , Poisson's ratio  $\nu = 0.2$ , and joint friction angle of  $65^\circ$ . Two recent DDA enhancements are utilized in the DDA version used here: (1) sequence excavation modeling capabilities (Tal et al., 2014), and (2) non-reflective boundaries (Bao et al., 2012).

The DDA mesh used for this verification is shown in Fig. 5 with the

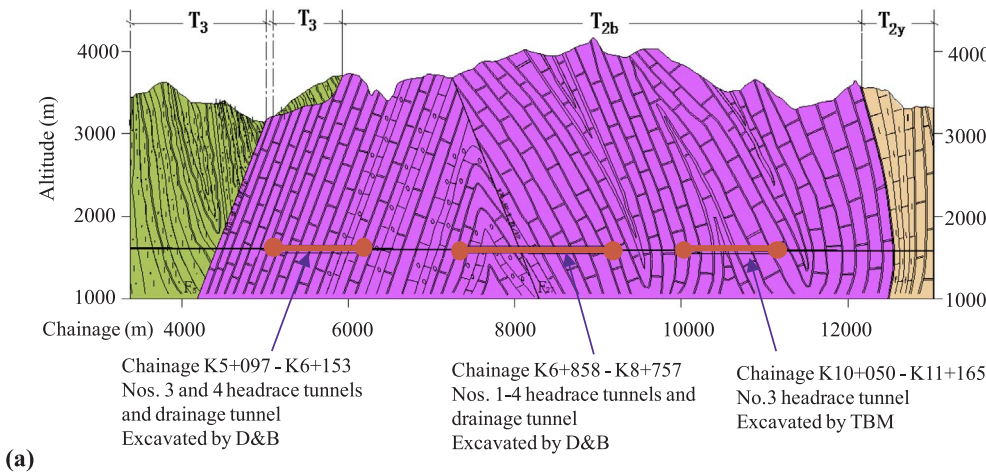
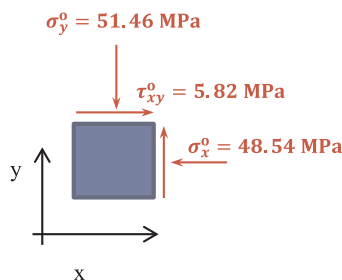
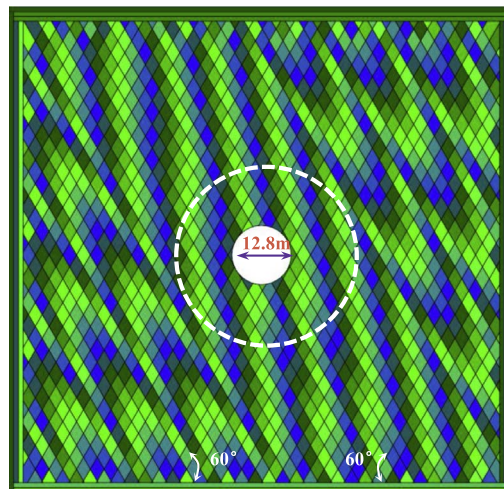


Fig. 11. (a) Geological cross section of No. 2 headrace tunnel at Jinping II hydropower station, (b) *in situ* stresses conditions at the site (Zhang et al., 2012b); (c) the representative DDA mesh with the affected zone delineated.

(a)



(b)



(c)

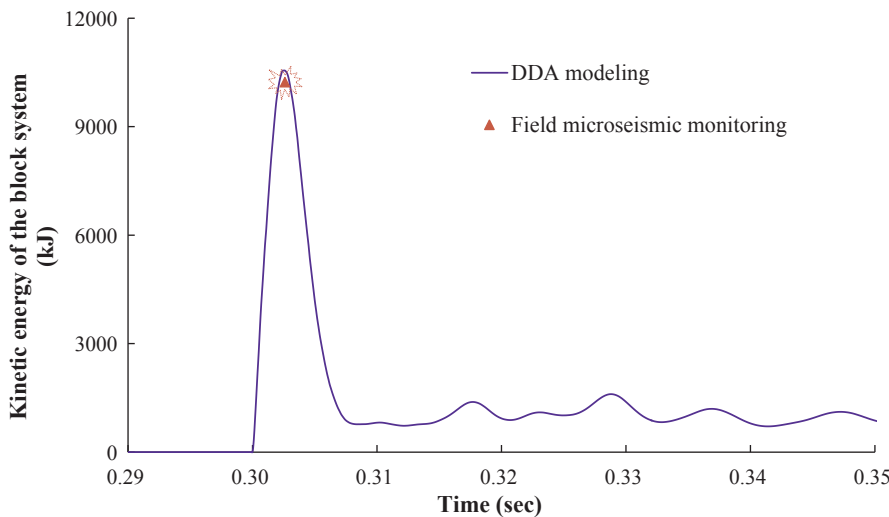


**Fig. 12.** Validation of the kinetic energy of the block system in the affected zone as computed with DDA using monitored micro seismicity at Jinping II hydropower station (micro-seismicity data from [Chen et al. \(2015\)](#)).

analyzed keyblock marked. The obtained acceleration, velocity, and displacement time histories are shown in [Fig. 6](#). As would be expected, once the space is formed the acceleration rapidly increases to  $3.4 \times 10^4 \text{ m/s}^2$ , and once the block is detached from the surrounding rock mass the acceleration immediately drops to zero ([Fig. 6a](#)). The velocity increases as the keyblock responds to the thrust from the boundary joints until it reaches steady state while the keyblock flies at constant velocity (recall gravity is ignored) in the tunnel space ([Fig. 6b](#)). The displacement time histories reflect this as well ([Fig. 6c](#)). As would be expected, the peak horizontal acceleration decreases with increasing block size ([Fig. 7](#) top panel). We find that the numerical error in DDA computations of peak horizontal acceleration is rather high (41%) when the keyblock area is small ( $0.038 \text{ m}^2$ ), but it decreases to 3% only for block area of  $0.85 \text{ m}^2$  ([Fig. 7](#) top panel). The relative error with respect to acceleration is:

$$E_n = \frac{|a_a - a_n|}{a_a} \times 100\% \tag{9}$$

The peak block acceleration may seem extremely high, but the obtained keyblock velocities are similar to velocities measured in the field. For example, [Kaiser and Cai \(2012\)](#) suggested that ejected rock fragments associated with rockbursts may travel at velocities in excess of 3 m/s; rockburst velocities upwards of 10 m/s were estimated by [Ortlepp and Stacey \(1994\)](#). Direct velocity measurements of ejected blocks using high-speed video camera in simulated rockburst experiments representing a 1600 m deep tunnel in South Africa suggest peak velocities in the range of 0.6–2.5 m/s ([Milev et al., 2001](#)). These field measurements are in agreement with our analytical and numerical results.

**2.3. Field verification**

Seismic waves generated during strong rockbursts propagate radially from the source in all directions. The emitted seismic energy is proportional to the integral of the sum of the *P* and *S* wave velocities ([Hudyma et al., 2003](#)) although observations from South African mines suggest that most of the seismic energy is contained in the *S*-waves ([Hedley, 1992](#)). The total seismic energy at distance *R* from the source to a measurement point can be estimated ([Mendecki et al., 2010](#)):

$$U_{p,s} = \frac{8}{5} \pi \rho v_{p,s} R^2 \int_0^{t_s} \dot{u}_{corr}^2(t) dt \tag{10}$$

where  $U_{p,s}$  is the total wave energy emitted from the micro seismic source ( $U_p$  and  $U_s$ ),  $\rho$  is the density of the rock,  $v_{p,s}$  is the *P* or *S* wave velocity,  $t_s$  is the duration of the seismic event, and  $\dot{u}_{corr}^2$  is the square of the far-field-corrected radiation pattern of the velocity pulse. The  $U_s/U_p$  ratio may be used as an indicator of the seismic source mechanism

([Urbancic et al., 1992](#); [Xiao et al., 2016](#)), i.e., tensile when  $U_s/U_p < 10$ , shear when  $10 \leq U_s/U_p \leq 20$ , and mixed mode when  $U_s/U_p > 20$ .

The radiated energy during monitored rockbursts in Jinping II Hydropower Station was calculated by [Chen et al. \(2015\)](#). The micro seismic sensors were installed in two arrays positioned at distances of 50–70 m and 100–120 m from the face, and were moved forward with

**Table 1**

Quantitative classification of rockburst intensity based on radiated seismic energy monitored at Jinping hydroelectric project tunnels (modified after [Feng et al. \(2012\)](#)).

Rockburst intensity	Log <sub>10</sub> (E)
None	(−∞, 0]
Weak	(0, 2]
Moderate	(2, 4]
Intense	(4, 7]
Extremely intense	(7, +∞]

Note: the seismic energy scale is logarithmic. Unit of E is Joule.

**Table 2**

Parameters of various numerical models.

Series	Case	Discontinuities joints			Young's modulus of intact rock <i>E</i> (GPa)	Monitored blocks
		Joint friction (μ)	Dip angle α (°)	Joint spacing <i>s</i> (m)		
1	a1	0.2	90	1.5	40	197
	a2	0.4	90	1.5	40	
	a3	0.6	90	1.5	40	
	a4	0.8	90	1.5	40	
	a5	1.0	90	1.5	40	
2	b1	0.7	30	1.5	40	102
	b2	0.7	45	1.5	40	
	b3	0.7	60	1.5	40	
	b4	0.7	75	1.5	40	
	b5	0.7	90	1.5	40	
3	c1	0.7	90	1.0	40	422
	c2	0.7	90	1.5	40	
	c3	0.7	90	2.0	40	
	c4	0.7	90	2.5	40	
4	d1	0.7	90	1.5	20	197
	d2	0.7	90	1.5	30	
	d3	0.7	90	1.5	40	
	d4	0.7	90	1.5	50	
	d5	0.7	90	1.5	60	

the advance of the working face (see Fig. 8). The natural frequency of the sensors was 14 Hz with reliable frequency domain between 7 Hz and 2000 Hz. A characteristic rockburst seismogram is displayed in Fig. 9 (e.g., Feng et al. (2016)) where the P and S wave arrivals are depicted and the total duration of the event can be inferred. From the known distance between the two arrays the characteristic P and S wave velocities of the rock mass can be obtained. The distance to the source can be determined by solving Eq. (10) for the two arrays, assuming the total seismic energy is equal in both arrays. Once the distance to the source is found, the total energy of the seismic event can be computed.

In order to assess the level of seismic energy associated with rockbursts in the field, consider the documented rockburst shown in Fig. 10, an intensive rockburst that was recorded in the early morning of February 23, 2011 at Stake K8 + 805–815 of No. 2 headrace tunnel in Jinping II hydroelectric project, while the micro-seismic monitoring arrays were in place and ready. Due to the difficult ground conditions, namely the medium strength of the rock and the high level of *in situ* stress, the rate of advance at that day was restricted to 2 m. The rockburst-induced tremor was felt by workers, and flying rock fragments damaged nearby vehicles. The total seismic energy computed for the entire day was  $10^7$  J (Chen et al., 2015).

We will use this case study to validate our theoretical and numerical predictions with regard to kinetic energy of the affected zone using the measured seismic energy by Chen et al. (2015) during the day that rockburst took place. Our DDA model is based on the typical cross section of the rock mass in Jinping II project where the studied rock burst took place (Fig. 11a). Note that while the rock mass structure is complicated, in the relevant section of the tunnel it can generally be characterized by two steeply inclined joint sets, the bedding planes that dip to the left of the cross section and the cross joints that dip to the

right. This rock mass pattern is simulated with DDA in a simplified manner using two joint sets dipping  $60^\circ$  to either side of the cross section with a mean spacing of 2.5 m (Fig. 11c). This generalized concept of the rock mass structure used for our DDA model is justified by results of two field studies (e.g., Li et al. (2012) and Li et al.(2017)).

Based on the work by Zhang et al. (Zhang et al., 2012b) the *in situ* stress components used in the two-dimensional DDA simulation are:  $\sigma_y^o = -51.46\text{MPa}$  and  $\tau_{xy}^o = 5.82\text{MPa}$  indicating that the vertical stress dominates at that location in the tunnel. According to both laboratory and field measurements, the mechanical parameters of the T<sub>2b</sub> marble lithology at the site are (Zhang et al., 2014): Young’s modulus  $E = 55.0\text{ GPa}$ , Poisson’s ratio  $\nu = 0.27$ , and joint friction  $\mu$  of 0.55 ( $\phi = 29.0^\circ$ ). These values are used as input in our DDA model.

The number of monitored blocks in the affected zone (delineated in Fig. 11c) is 145. The obtained kinetic energy with DDA is 5276 kJ. This result applies to the two dimensional case where the tunnel extends 1 m in length. In reality, the tunnel was excavated to a distance of 2 m during that day. To allow a meaningful comparison between the monitored and DDA results, the numerically obtained kinetic energy must be multiplied by a factor of 2.0. The corrected kinetic energy response in time domain as obtained with DDA is shown in Fig. 12. The total seismic energy monitored in the field during that day is compatible to the total kinetic energy of the block system in the affected domain as predicted with DDA.

The monitored seismic energy in the recorded and analyzed event at Jinping falls into the “extremely intense” category according to Feng’s rockburst hazard classification (Table 1). Similar intensities were recorded in Northern Ural bauxite mine in Russia using a monitoring seismic network, where the largest tremors were characterized by seismic energy in the order of  $10^7 \sim 10^8$  J (Voinov et al., 1987). These

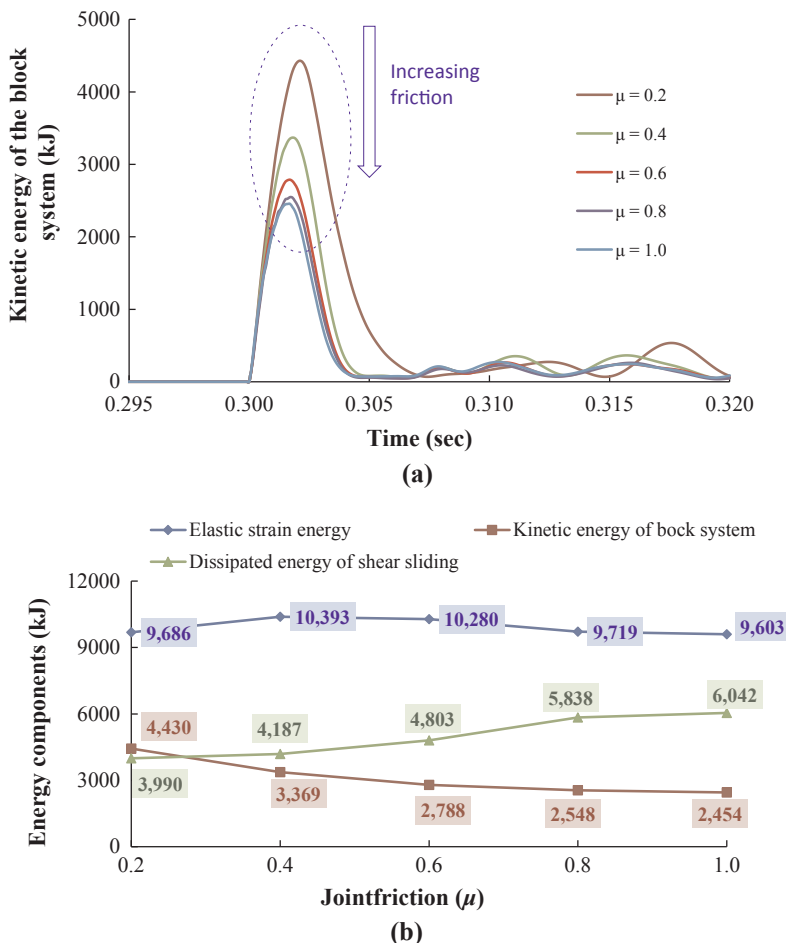


Fig. 13. Influence of joint friction: (a) evolution of kinetic energy of the block system in affected zone; (b) energy component distribution.

results confirm the predictive capability of DDA with respect to rockburst hazard, as scaled by the total kinetic energy of the block system in the affected zone.

### 3. Influence of rock mass parameters on rockburst energy

It is widely accepted that fractured and jointed rock masses are more prone to rockburst hazard, particularly in high *in situ* stress regimes (e.g., Miao et al. (2016)). Discontinuous rock masses are typically comprised of finite blocks formed by the intersection of pre-existing joints. We investigate in this section the influence of individual rock mass parameters such as joint friction ( $\mu$ ), dip angle ( $\alpha$ ), joint spacing ( $s$ ), and Young’s modulus of intact rock ( $E$ ), on the components of energy redistribution.

#### 3.1. Boundaries of modeled domain

We will use DDA to perform a sensitivity analysis of these parameters. To limit the number of discrete blocks involved in this dynamic process we constrain our analysis to the “Rockbursting Prone Zone” that extends to a distance of 1.5 tunnel diameters from the tunnel center. As presented by He et al. (2016), 59% of the total energy increase occurs within this annulus. Although it would have been better to extend the analyzed domain to a distance of three diameters from the tunnel center, modeling the deformation of each and every block in the case of smallest joint spacing considered in our sensitivity analysis (1 m) will amount to monitoring 1793 blocks for a tunnel radius of  $a = 4$  m. We do not feel such an effort is justified as the difference in energy change between 1.5D and 3.0D is not very large (see He et al. (2016)). Moreover, our choice of modeled domain size of 1.5D is supported by field monitoring of the excavation damage zone (EDZ) at Jinping II

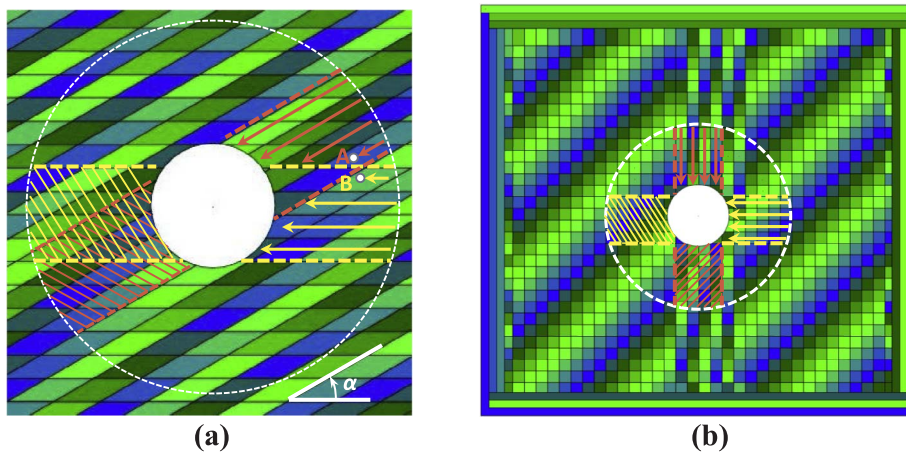
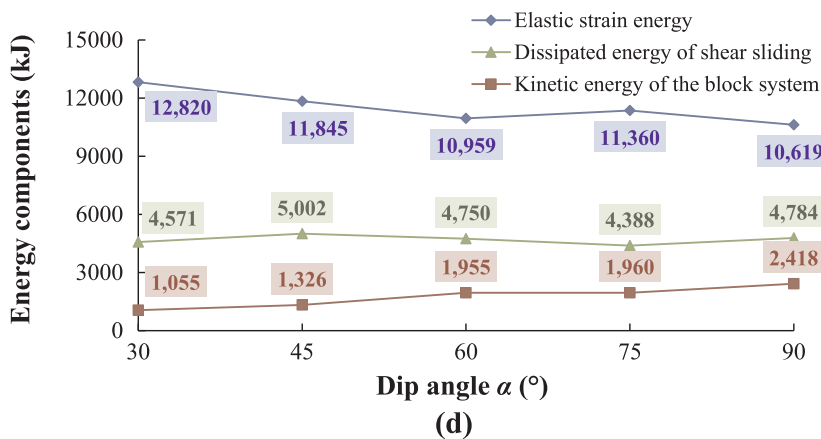
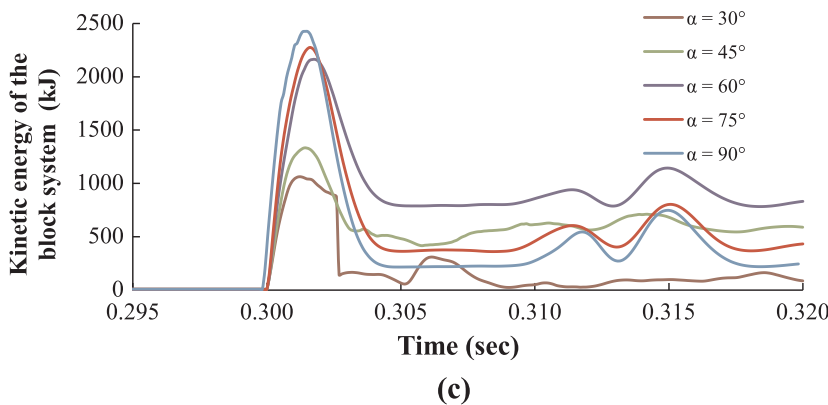


Fig. 14. Influence of joint inclination: (a) slip trajectory of blocks in the affected domain where  $\alpha = 30^\circ$ ; (b)  $\alpha = 90^\circ$ ; (c) evolution of kinetic energy of the block system in affected zone; (d) energy component distribution.



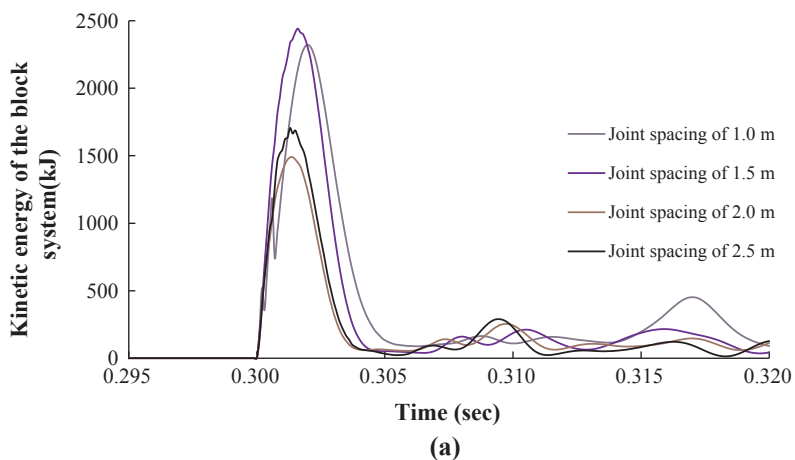
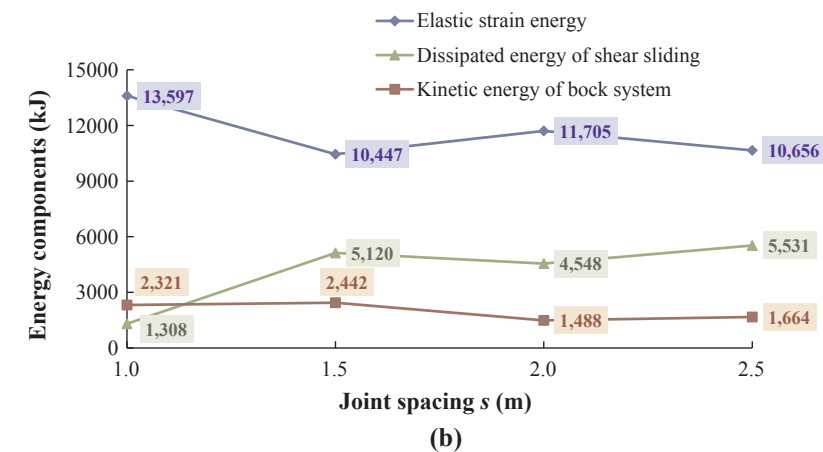


Fig. 15. Effect of joint spacing: (a) time-histories of kinetic energy of the block system in affected zone; (b) distribution of energy components.



Hydropower station using pre-installed digital borehole camera (Li et al., 2011). The depth of the EDZ in the No. 3 headrace tunnel was found to be 2.7 m, namely 0.72D from the tunnel center, much less than the modeled domain of 1.5D considered in our analysis here.

Considering Fig. 1, the analyzed domain radius  $b$  now equals  $1.5D$ . Once the space of the excavation is created, the energy increase must be balanced by three energy components in the block system covering the analyzed domain (He et al., 2016):

$$U_B^0 + 1.59 \times U_A^0 = U_{e,B}^* + U_{k,B}^* + U_{s,B}^* \tag{11}$$

where  $U_{e,B}^*$  is strain energy,  $U_{k,B}^*$  is kinetic energy of the block system associated with the instantaneous motion of discrete blocks, and  $U_{s,B}^*$  is

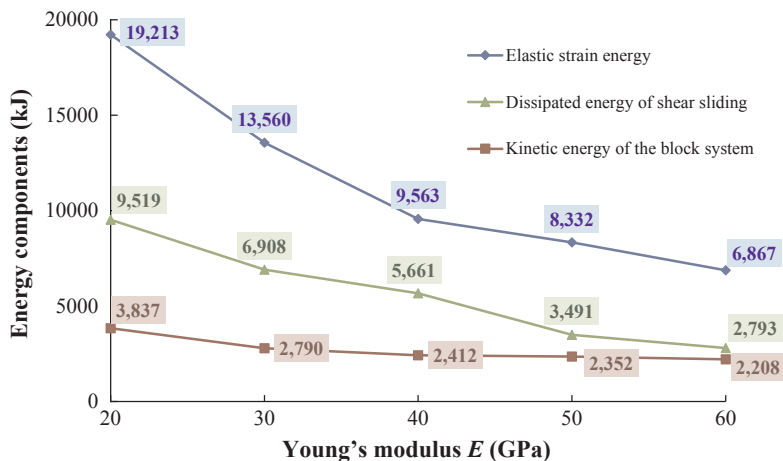


Fig. 16. Influence of Young's modulus on the energy component distribution.

Table 3 Correlation of GSI, RMR and Q rock mass classification systems.

Approach	Equation
Bieniawski (1976)	$RMR = 9 \ln Q + 44$
Hoek et al. (1995)	$GSI = RMR_{76}$ (use of 1976 version of RMR)
Hoek et al. (1995)	$GSI = RMR_{89} - 5$ (use of 1989 version of RMR)
Hoek et al. (1995)	$GSI = 9 \ln Q' + 44$ ( $Q' = \frac{RQD}{J_n J_a}$ )
Ünal (1996)	$M-RMR = 9.66 \ln Q + 37.9$

GSI		Very good Very rough, fresh unweathered surfaces	Good Rough, slightly weathered, Iron stained surfaces	Fair Smooth, moderately weathered or altered surfaces	Poor Slitkensisided, highly weathered surfaces with compact coating or fillings of angular fragments	Very poor Slitkensisided, highly weathered surfaces w soft clay coatings or fillings
	INTACT OR MASSIVE – intact rock specimens or massive in situ rock with few widely spaced discontinuities	80			N/A	N/A
	BLOCKY – very well interlocked undisturbed rock mass consisting of cubical blocks formed by three orthogonal discontinuity sets		70			
	VERY BLOCKY – interlocked, partially disturbed rock mass with multifaceted angular blocks formed by four or more discontinuity sets		60	50		
	BLOCKY/DISTURBED – folded and/or faulted with angular blocks formed by many intersecting discontinuity sets					
	DISINTEGRATED – poorly interlocked, heavily broken rock mass with a mixture of angular and rounded pieces					

Decreasing interlocking of rock pieces  
↓

Fig. 17. The range of GSI values relevant to rockburst hazard scaling in this paper (GSI table modified after Hoek and Brown (1997)).

dissipated energy due to frictional sliding along pre-existing joints in the analyzed domain.

The kinetic energy of the block system can be obtained using DDA by summing the kinetic energies of all individual blocks in the analyzed domain:  $U_{k,B}^* = \sum_{i=1}^n \frac{1}{2} m_i v_i^2$ , where  $n$  is the number of monitored blocks,  $m_i$  and  $v_i$  are the mass and velocity of each block in the modeled domain as computed with DDA. Similarly, the strain energy is found by recording the stresses computed with DDA at the centroid of each block:  $U_{e,B}^* = \sum_{i=1}^n \phi_i A_i$ , where  $\phi_i$  and  $A_i$  are the strain energy density and area of block  $i$  in the DDA mesh for the modeled domain. The difference between the total energy and the sum of strain energy and kinetic energy is the energy dissipated by shear sliding along joints, readily determinable by Eq. (11).

### 3.2. Effect of individual rock mass parameters

To study the relative significance of the four individual rock mass parameters outlined above ( $\mu, \alpha, s, E$ ) we simulate different scenarios

with forward DDA modeling as listed in Table 2, keeping in all simulations an initial *in situ* hydrostatic stress level of  $p = 45\text{MPa}$ . The different scenarios studied are grouped into four series where all meshes are comprised of two joint sets, one of which maintains horizontal and the other is inclined at dip angle  $\alpha$ . In series 1, the effect of joint friction is considered ( $\mu = 0.2, 0.4, 0.6, 0.8,$  and  $1.0$ ) while keeping all other rock mass parameters constant. The evolution of the kinetic energy of the block system in the modeled domain ( $U_{k,B}^*$ ) as a function of joint friction  $\mu$  over time is plotted in Fig. 13a. Once the excavation space is formed the kinetic energy spikes, a dynamic process that must be accompanied by strong tremor that may generate keyblock ejections, provided that joint friction is sufficiently low. The influence of joint friction on the three energy components is illustrated in Fig. 13b: while the kinetic energy decreases with increasing joint friction by 51%, the dissipated energy increases by 45% over the studied friction range, while the elastic strain energy remains virtually the same.

The influence of joint inclination is examined in series 2 where  $\alpha$  is changed from  $30^\circ$  to  $90^\circ$  at  $15^\circ$  intervals while keeping the other joint

Table 4  
Input parameters for DDA representing various GSI qualities.

GSI	Joint set No.	Dip/dip direction	Total number of blocks	Spacing (m)	Length (m)	Bridge (m)	Joint friction (°)	Rock mass modulus $E_{rm}$ (GPa)	Intact modulus $E_i$ (GPa)	RD
50	4	0°/0°	12,442	2.0	60	0.20	25	9	30	0.5
55		20°/90°	7943	2.5	55	0.25	27	14	34	
		80°/270°								
60	3	0°/0°	2789	3.0	50	0.30	30	20	39	
65		20°/90°	2001	3.5	45	0.35	32	29	45	
70		80°/270°	1525	4.0	40	0.40	35	39	53	
75			1124	4.5	35	0.45	38	50	61	
80		20°/90°	819	5.5	30	0.50	40	61	69	
		80°/270°								

set horizontal (Fig. 14a and b), and the friction coefficient on both joint sets is kept constant at 0.7. The kinetic energy response to joint inclination is illustrated in Fig. 14c, where maximum kinetic energy is recorded for the case of vertical joints ( $\alpha = 90^\circ$ ) and the minimum kinetic energy is recorded for the shallowest joint inclination of  $30^\circ$ .

To explain this finding consider Fig. 14a and b and the delineated zones of possible block motion in the affected zone. In the orthogonal jointing configuration (Fig. 14b), the motion of blocks by sliding along horizontal joints does not restrict block motion along vertical joints, namely all blocks in the delineated areas are free to slide into the opening space, if the energy is sufficiently high and the joint friction is sufficiently small. In the case of inclined joints, however, the motion of blocks along horizontal joints (see for example block B in the Fig. 14a) is restricted by motion that must first take place on inclined joints (e.g., block A in Fig. 14a). This overlapping of removable areas around the tunnel restricts the kinematical freedom of blocks to slide into the opening once the space is formed, even if sufficient energy is provided

and if joint friction is sufficiently small. This “interlocking effect” that constrains block motion appears to increase with decreasing dip of the inclined joint set. The effect of dip angle on the other two energy components is illustrated in Fig. 14d.

The influence of block size, as scaled by the joint spacing  $s$ , is studied in series 3 of Table 2 and is demonstrated in Fig. 15. As would be expected intuitively, the kinetic energy of the block system increases with decreasing block size (Fig. 15a) whereas the dissipated energy due to shear sliding increases with increasing block size (Fig. 15b).

The influence of Young’s modulus of intact rock, from 20 GPa to 60 GPa, is studied in series 4 of Table 2 and the results are plotted in Fig. 16. All energy components decrease with increasing Young’s modulus, with the elastic strain energy decreasing by 64%, the dissipated energy by 71%, and the excavation-induced kinetic energy by 42%. The initial strain energy density stored in the rock mass before the excavation is formed ( $\phi_o$ ) is inversely proportional to Young’s modulus  $E$ :

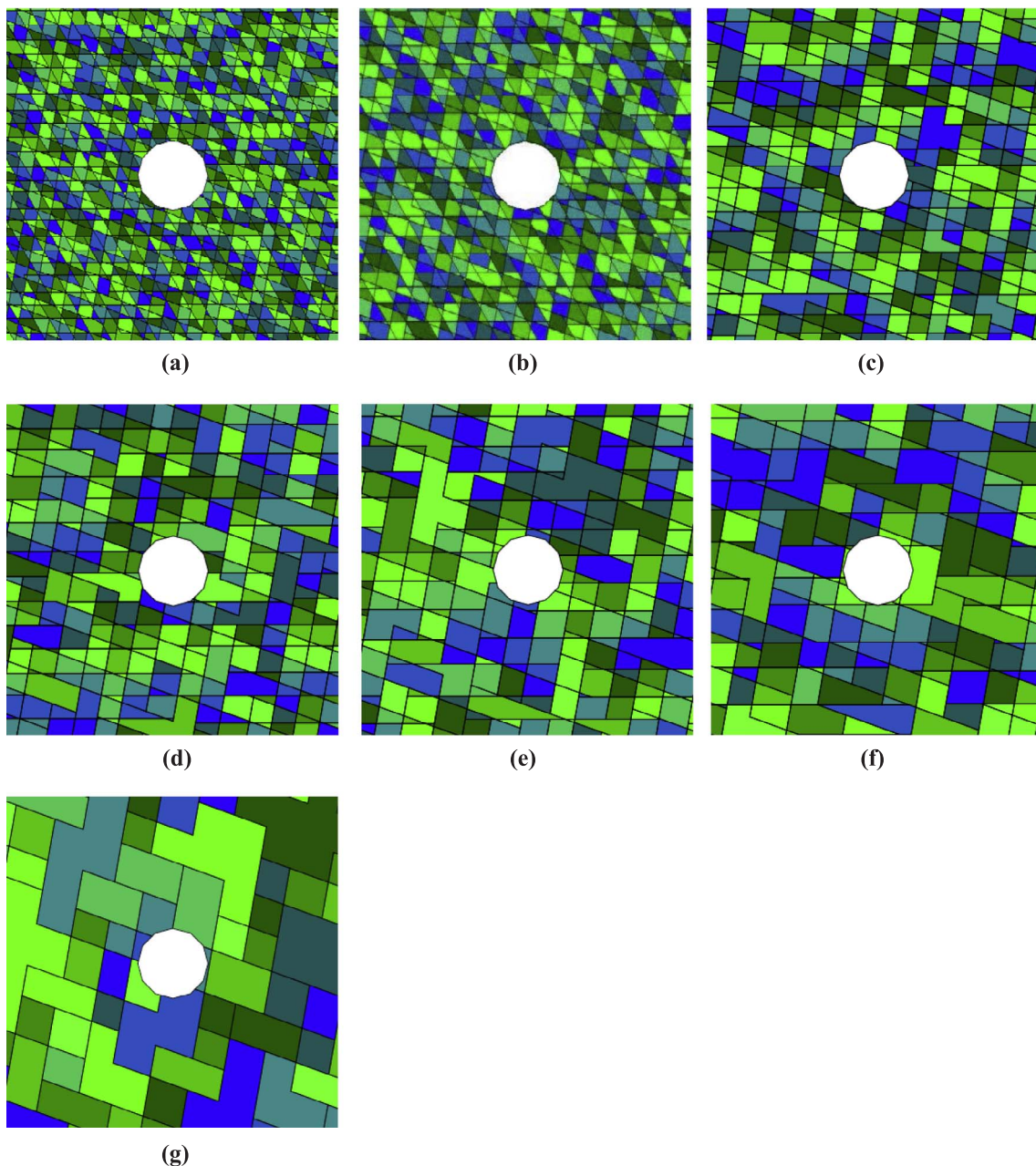


Fig. 18. Blow-up view of DDA block systems used to represent various GSI qualities: (a) GSI = 50; (b) GSI = 55; (c) GSI = 60; (d) GSI = 65; (e) GSI = 70; (f) GSI = 75; (g) GSI = 80.

$$\phi_0 = \frac{1}{2E} \sum_{i=1}^3 \sigma_i^0 \varepsilon_i^0 \quad (12)$$

where  $\sigma_i^0$  and  $\varepsilon_i^0$  are initial principal stresses and strains. Consequently, the magnitude of total energy release once the space is formed decreases with increasing Young's modulus, and this is reflected by the simultaneous decrease of all energy components with increasing rock mass stiffness.

#### 4. Discussion

We have shown the kinetic energy associated with rockbursts is inversely related to the frictional resistance of discontinuities. Further probing into the role of the main characteristics of the rock mass reveals that all energy components decrease with increasing stiffness of intact rock elements. The kinetic energy of the blocks in the affected zone decreases with increasing joint spacing (or with increasing block size), and increases with increased inclination of the unfavorable joint set. These findings lead us to an attempt to address rockburst hazard underground, as scaled by the total kinetic energy of the block system in the affected zone, in terms of rock mass quality, as scaled by GSI.

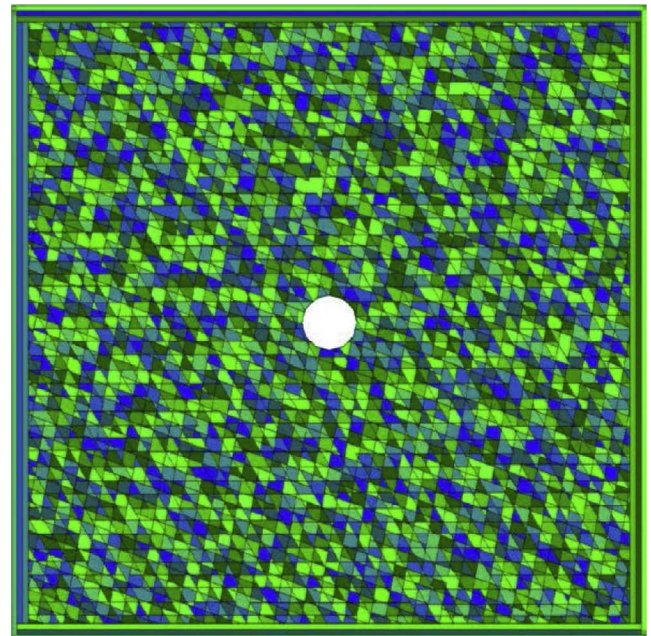
##### 4.1. Influence of rock mass quality

Several empirical rock mass classification methods are currently in use in rock engineering including the Q (Barton et al., 1974), RMR (Bieniawski, 1973), and GSI (Hoek and Brown, 1997), and some useful correlations among them are listed in Table 3. Based on our understanding of the relationship between individual rock mass parameters and energy redistribution as discussed above, we will attempt to investigate here the relationship between rock mass quality, as scaled by GSI, and rockburst potential, so as to provide rockburst hazard scaling in the relevant rock masses.

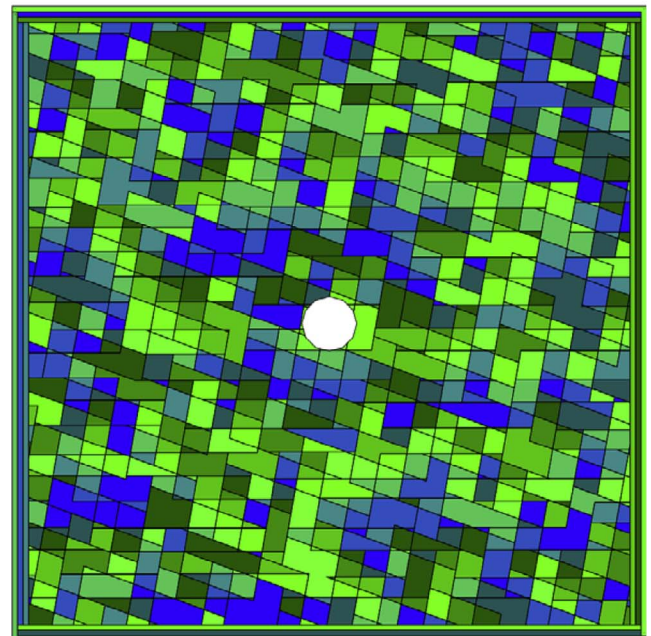
An interesting point about rockbursts is that they do not occur in weak rocks; rock masses prone to rockbursts are typically stiff, strong, and brittle, with uniaxial compressive strength of 100–400 MPa and rock mass modulus  $E_{rm}$  greater than 20 GPa (Obert and Duvall, 1967), as recently confirmed in field studies at Jinping II hydroelectric power station (e.g., Zhang et al. (2014)).

To try and constrain the rock mass quality levels at which rockbursts can be expected we generate seven block systems with DDA that represent rock mass qualities ranging from “Poor Rock” to “Good Rock” GSI categories (see Fig. 17), with input data listed in Table 4. A blow-up view close to the tunnel of the seven rock masses as modeled with DDA is shown in Fig. 18; the entire meshes of two representative cases for GSI 50 and 75 are shown in Fig. 19. We use the available capability in DDA for random generation of structural parameters such as joint spacing, length, and bridge (degree of randomness) so as to obtain a more realistic representation of a real geological rock mass. Forward DDA modeling is performed in all cases under an assumed initial hydrostatic stress of 55 MPa and with Young's modulus for intact rock assumed for the DDA blocks. The dimension of the DDA mesh is 110 m (width)  $\times$  110 m (height) and the diameter of the circular tunnel is 10 m.

The kinetic energy of the block system in the affected domain is plotted in Fig. 20a. It is apparent that rock mass quality with a GSI of 60 is the most prone to rock bursting, with upwards of 5350 kJ of kinetic energy associated with excavation-induced block motion. The kinetic energy declines appreciably by 56% to 2346 kJ with GSI reaching 65, and continues to drop further with increasing rock mass quality. The influence of rock mass quality on the kinetic energy of the blocks in the rock mass can be appreciated better by inspection of Fig. 20b where both the two other energy components clearly exhibit decrease with increasing rock mass quality, whereas the kinetic energy exhibits a maxima around GSI = 60 (note that the energy axis scale in Fig. 20b is logarithmic). As would be expected, the elastic strain energy is



(a)



(b)

Fig. 19. Two examples of complete DDA block systems: (a) GSI = 55 with four orthogonal joint sets; (b) GSI = 75 with three orthogonal joint sets.

inversely proportional to the rock mass quality due to the influence of Young's modulus which increases with GSI as does the dissipated energy by shear due to the increased block size with increasing GSI.

##### 4.2. Field evidence

A rockburst hazard classification using seismic energy has been proposed by Feng et al. (2012) based on 133 documented rockburst events that occurred in the course of excavation of the Jinping tunnels (Table 1). The system of tunnels, consisting of four headrace tunnels, two auxiliary tunnels, and one drainage tunnel, was driven under an extremely high overburden reaching 1500 m along 75% of the 16.7 km length of the tunnels, and reaching a maximum of 2525 m at the

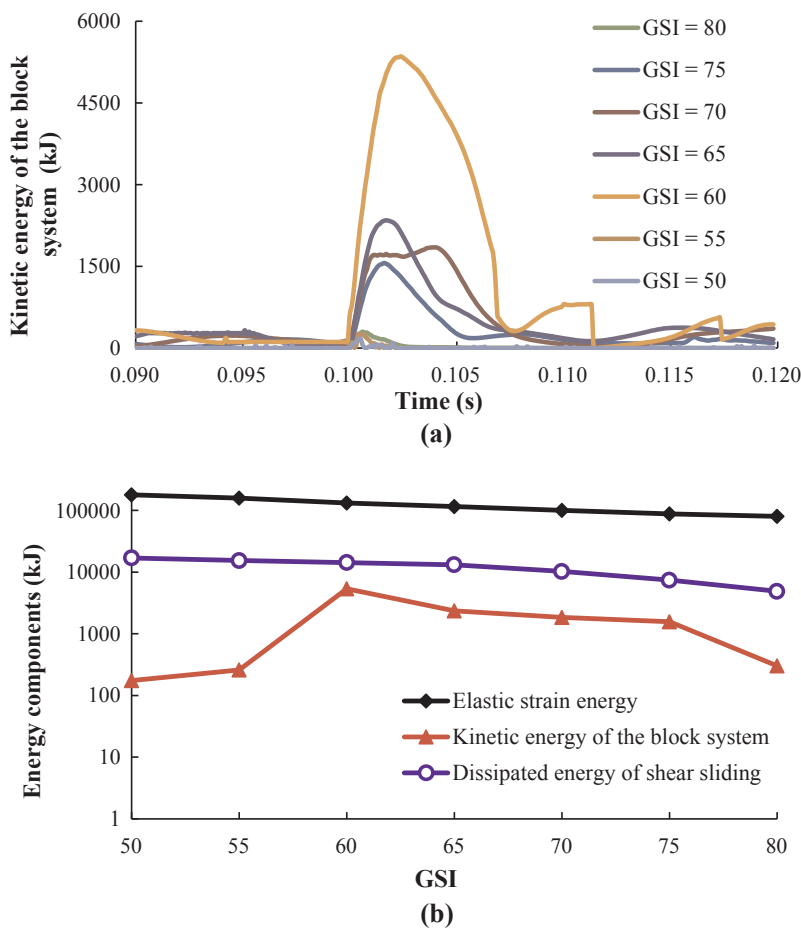


Fig. 20. Effect of rock mass quality as scaled by DDA and GSI on energy components: (a) kinetic energy time-histories of the block system in affected zone; (b) energy component distribution.

deepest point. The rock mass is comprised of medium strength and highly discontinuous marble with an estimated GSI value ranging between 55 and 75 (Smading et al., 2009). Although the field observations were recorded using the Chinese rock mass classification (TB10003-2005, 2005), they can readily be converted to GSI (see Table 5). Most rockbursts were triggered in tunnel stretches with rock mass modulus  $E_{rm}$  from 20 GPa to 55 GPa (He et al., 2012; Liu et al., 2011; Zhang et al., 2014), corresponding to GSI values in the range of 60 and 75 in our analysis (see Table 4), in agreement with our expectations.

Representative cases of moderate, intensive, and extremely intensive rockbursts as defined in Table 6 are illustrated in Fig. 21. Approximately 88% of 300 recorded rockburst events documented in the course of excavation of Jinping tunnels (Feng et al., 2013) occurred in a “blocky” rock structure (see Fig. 22) with uniaxial compressive strength of  $\sigma_c = 100\text{--}140$  MPa (Liu et al., 2016). Furthermore, only 12% of rockbursts occurred in “intact/massive” structure and no rockbursts were recorded in rock mass structures defined as “disintegrated”. These field evidences are in agreement with our assessment that rock mass qualities between GSI = 60–75 are most prone to rockburst hazard.

Table 6 Representative rockbursts documented during excavation of Jinping II hydroelectric station.

Intensity	Date	Chainage	CRMC*	Depth (m)	Tunnel	Reference source
Moderate	Jan. 13, 2011	K8 + 810 ~ 870	II	2490	No.2 headrace tunnel	
Moderate	Apr. 5, 2011	K6 + 152 ~ 160	Mainly III; partly II	2000 ~ 2130	No.3 headrace tunnel	Chen et al. (2015)
Moderate	Apr. 16, 2011	K5 + 560 ~ 540	Mainly II; partly III	2000 ~ 2114	No.4 headrace tunnel	Zhang et al. (2012a)
Intensive	Aug. 12, 2011	K8 + 827 ~ 852	Mainly III; partly II	2344 ~ 2442	No.4 headrace tunnel	Chen et al. (2015)
Intensive	Nov. 26, 2011	K5 + 750 ~ 790	Mainly II; partly III	2050	No.3 headrace tunnel	
Extremely intensive	Apr. 16, 2011	K6 + 025 ~ 045	Mainly III; partly II	2000 ~ 2114	No.4 headrace tunnel	Chen et al. (2015)

Note: CRMC\* is referred to as Chinese rock mass classification (TB10003-2005, 2005).

Stress-based criteria have been proposed for rockburst classification (see Table 7). Although these criteria may be useful in the preliminary design stage, in practice, applying these criteria to a single rockburst event might lead to inconsistencies in the rockburst classification (Zhao et al., 2017). Nevertheless, as can be appreciated from inspection of Table 7, rockburst intensity decreases with increasing ratio between the uniaxial compressive strength  $\sigma_c$  and the magnitude of in-situ stress, which is in general agreement with our model.

Table 5 Conversion of Chinese rock mass classification (TB10003-2005, 2005) used at Jinping to GSI.

“GSI” method	$\geq 81$	80 ~ 61	60 ~ 41	40 ~ 21	< 21
China rock mass classification (CRMC)	I	II	III	IV	V
					VI

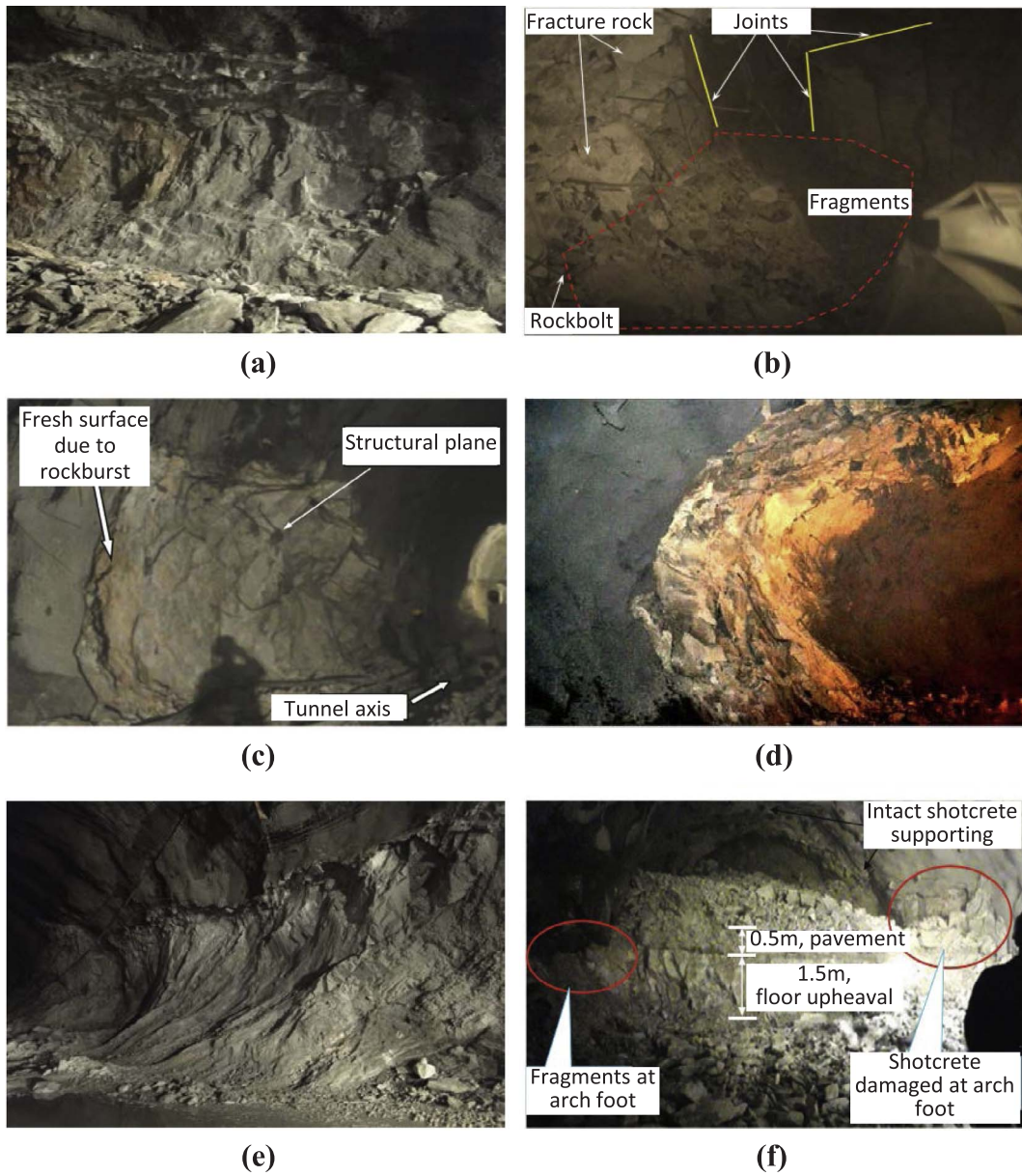


Fig. 21. Documented rockbursts during excavation of Jinping II hydroelectric power station: (a) moderate rockburst on January 13, 2011 in No. 2 headrace tunnel; (b) moderate rockburst on April 5, 2011 in No. 3 headrace tunnel (Chen et al., 2015); (c) moderate rockburst on April 16, 2011 in No. 4 headrace tunnel (Zhang et al., 2012a); (d) intensive rockburst on August 12, 2011 in No. 4 headrace tunnel (Chen et al., 2015); (e) intensive rockburst on November 26, 2011 in No. 3 headrace tunnel; (f) extremely intensive rockburst on April 16, 2011 in No. 4 headrace tunnel (Chen et al., 2015).

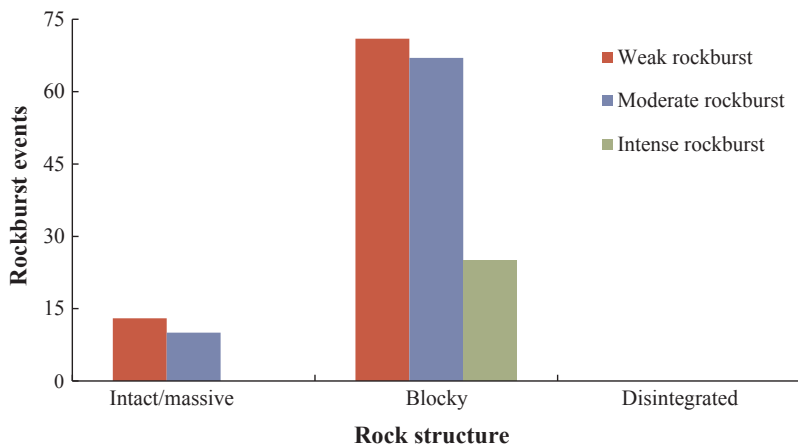


Fig. 22. Relationships between rockburst events and rock structure based on field observation during drill and blast excavation at Jinping II hydroelectric project (modified after Feng et al. (2013)).

**Table 7**  
Comparison of stress-based criteria of predicting rockburst classification.

Criterion	Details of criteria					Assumption
Barton et al. (1974)	Ratio	$\sigma_c/\sigma_1 > 5$	$2.5 < \sigma_c/\sigma_1 \leq 5$		$\sigma_c/\sigma_1 \leq 2.5$	$\lambda = 0.5 \sim 1$
	Intensity	No	Light rockburst		Heavy rockburst	
Russenes (1974)	Ratio	$\sigma_{\gamma\gamma}/\sigma_c < 0.2$	$0.2 \leq \sigma_{\gamma\gamma}/\sigma_c < 0.3$	$0.3 \leq \sigma_{\gamma\gamma}/\sigma_c < 0.55$	$\sigma_{\gamma\gamma}/\sigma_c \geq 0.55$	$\sigma_c/Is^* = 20$
	Intensity	No	Light rockburst	Moderate rockburst	Strong rockburst	
Hoek and Brown (1980)	Ratio	$\sigma_c/\sigma_v > 7$	$\sigma_c/\sigma_v = 3.5$	$\sigma_c/\sigma_v = 2$	$\sigma_c/\sigma_v = 1.7$	$\sigma_c/\sigma_v = 0.5$
	Intensity	Stable	Minor sidewall spalling	Severe spalling	Heavy support required	Severe rockburst
Turchaninov et al. (1972)	Ratio	$(\sigma_{\gamma\gamma} + \sigma_{\perp})/\sigma_c \leq 0.3$	$0.3 < (\sigma_{\gamma\gamma} + \sigma_{\perp})/\sigma_c \leq 0.5$	$0.5 < (\sigma_{\gamma\gamma} + \sigma_{\perp})/\sigma_c \leq 0.8$	$(\sigma_{\gamma\gamma} + \sigma_{\perp})/\sigma_c > 0.8$	N/A
	Intensity	No rockburst	Possible rockburst	Certainly rockburst	Serious rockburst	

Note:  $Is^*$  refers to rock point load;  $\lambda$  is initial field stress ratio, and other notations are the same as in Section 1.

**5. Conclusions**

- An analytical solution of the local energy density around a circular tunnel in a linear elastic continuous and homogenous medium is derived to demonstrate the significance of principal stress ratio and material parameters on the result.
- We derive the peak acceleration of ejected blocks to explore the causative mechanism of rockbursts. The magnitude of acceleration obtained analytically is in agreement with results obtained with the numerical DDA method, and our results are also consistent with field measurements reported in the literature.
- We validate our DDA predictions using monitored seismic energy emissions detected during a typical intensive rock burst episode recorded while excavating the Jinping II hydroelectric project tunnels. Our results compare well with field measurements, suggesting that DDA can be a reliable tool to predict rockburst hazard underground.
- Based on DDA modeling, we study the relative significance of Young’s modulus, joint orientation, joint friction, and joint spacing on the energy components, i.e., the elastic strain energy, the

dissipated energy by shear sliding, and the kinetic energy of the rock blocks in the affected zone. We find that the kinetic energy of ejected keyblocks, or rockburst, decreases with increasing Young’s modulus, joint friction, and average block size.

- By simulating various rock mass qualities corresponding to GSI values between 55 and 80, we find that rockburst hazard, as scaled by the kinetic energy of the block system in the affected zone, is most severe between GSI values of 60–75. This result is supported by rockburst events documented during excavation of the Jinping II hydroelectric power station.

**Acknowledgments**

We thank Israel Commission for Higher Education for a post-doctoral fellowship awarded for excellent doctoral students from China (No. 850203241) through Ben-Gurion University of the Negev – Israel to Ben-Guo He. Y. Hatzor wishes to thank the Chinese Academy of Sciences – China for a visiting professorship grant awarded to senior international scientists (No. 2011T2G29).

**Appendix A. Derivation of Eq. (6)**

The rotation matrix from polar to rectangular coordinate systems (Fig. A.1) is (e.g., refer to Sadd (2009)):

$$Q_{ij} = \begin{bmatrix} \cos\theta & -\sin\theta \\ \sin\theta & \cos\theta \end{bmatrix} \tag{A.1}$$

Employing the second-order matrix transformation of isotropic tensor  $Q_{ij}$  from polar to rectangular coordinate systems, we obtain:

$$\sigma^*(x,y) = Q_{ij} \times \sigma^*(r,\theta) \times Q_{ij}^T$$

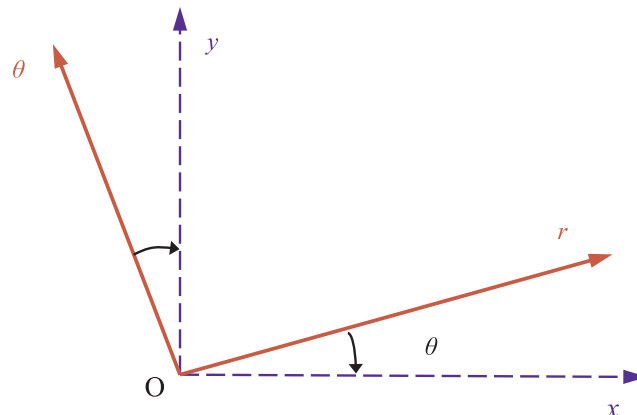


Fig. A.1. Transformation from polar to rectangular coordinates.

$$\begin{bmatrix} \sigma_x^* & \tau_{xy}^* \\ \tau_{yx}^* & \sigma_y^* \end{bmatrix} = \begin{bmatrix} \cos\theta & -\sin\theta \\ \sin\theta & \cos\theta \end{bmatrix} \begin{bmatrix} \sigma_r^* & \tau_{r\theta}^* \\ \tau_{\theta r}^* & \sigma_\theta^* \end{bmatrix} \begin{bmatrix} \cos\theta & -\sin\theta \\ \sin\theta & \cos\theta \end{bmatrix}^T \tag{A.2}$$

Using Eq. (A.2), the stress components  $(\sigma_x^*, \sigma_y^*, \tau_{xy}^*)$  in rectangular coordinate system can be expressed as follows:

$$\begin{cases} \sigma_x^* = \cos^2\theta\sigma_r^* - \sin 2\theta\tau_{r\theta}^* + \sin^2\theta\sigma_\theta^* \\ \sigma_y^* = \sin^2\theta\sigma_r^* + \sin 2\theta\tau_{r\theta}^* + \cos^2\theta\sigma_\theta^* \\ \tau_{xy}^* = \frac{1}{2}\sin 2\theta(\sigma_r^* - \sigma_\theta^*) + \cos 2\theta\tau_{r\theta}^* \end{cases} \tag{A.3}$$

Substituting Kirsch solution of Eq. (2) into Eq. (A.3) yields:

$$\begin{cases} \sigma_x^* = \frac{\sigma_1^0 + \sigma_2^0}{2} \left(1 - \frac{a^2}{r^2} \cos 2\theta\right) + \frac{\sigma_1^0 - \sigma_2^0}{2} \left(1 - \frac{4a^2}{r^2} \cos 3\theta \cos \theta + \frac{3a^4}{r^4} \cos 4\theta\right) \\ \sigma_y^* = \frac{\sigma_1^0 + \sigma_2^0}{2} \left(1 + \frac{a^2}{r^2} \cos 2\theta\right) - \frac{\sigma_1^0 - \sigma_2^0}{2} \left(1 + \frac{4a^2}{r^2} \sin 3\theta \sin \theta + \frac{3a^4}{r^4} \cos 4\theta\right) \\ \tau_{xy}^* = \frac{\sigma_1^0 - \sigma_2^0}{2} \times \frac{a^2}{r^2} \sin 2\theta + \frac{\sigma_1^0 - \sigma_2^0}{2} \left(-\frac{2a^2}{r^2} + \frac{3a^4}{r^4}\right) \sin 4\theta \end{cases} \tag{A.4}$$

Inspection of Eq. (A.4) reveals that the stresses after excavation are function of both position  $(r, \theta)$  and initial principal stresses  $(\sigma_1^0$  and  $\sigma_2^0)$ . Substituting Eq. (A.4) into Eq. (5) and then setting three angles for the horizontal, spandrel, and vertical paths  $(\theta = 0, \pi/4, \text{ and } \pi/2)$ , we can now obtain the energy density at various positions along these radial directions:

$$\begin{aligned} \varphi_{\text{Sidewall}, \theta=0}^* &= \frac{1+\nu}{2E} \left\{ (1-\nu) \left[ \sigma_1^0 + \sigma_2^0 - 2(\sigma_1^0 - \sigma_2^0) \frac{a^2}{r^2} \right]^2 \right. \\ &\quad - 2 \left( 1 - \frac{a^2}{r^2} \right) \left[ \frac{(\sigma_1^0 + \sigma_2^0)^2}{4} \left( 1 + \frac{a^2}{r^2} \right) - \frac{\sigma_1^{02} - \sigma_2^{02}}{2} \frac{a^2}{r^2} \left( 1 + \frac{3a^2}{r^2} \right) \right. \\ &\quad \left. \left. - \frac{(\sigma_1^0 - \sigma_2^0)^2}{4} \left( 1 - \frac{3a^2}{r^2} \right) \left( 1 + \frac{3a^4}{r^4} \right) \right] \right\} \\ \varphi_{\text{Spandrel}, \theta=\frac{\pi}{4}}^* &= \frac{1+\nu}{2E} \left[ (1-\nu)(\sigma_1^0 + \sigma_2^0)^2 - \frac{(\sigma_1^0 + \sigma_2^0)^2}{2} \left( 1 - \frac{a^4}{r^4} \right) + \frac{(\sigma_1^0 - \sigma_2^0)^2}{2} \left( 1 - \frac{a^2}{r^2} \right)^2 \left( 1 + \frac{3a^2}{r^2} \right)^2 \right] \\ \varphi_{\text{Roof}, \theta=\frac{\pi}{2}}^* &= \frac{1+\nu}{2E} \left\{ (1-\nu) \left[ \sigma_1^0 + \sigma_2^0 + 2(\sigma_1^0 - \sigma_2^0) \frac{a^2}{r^2} \right]^2 \right. \\ &\quad \left. - 2 \left( 1 - \frac{a^2}{r^2} \right) \left[ \frac{(\sigma_1^0 + \sigma_2^0)^2}{4} \left( 1 + \frac{a^2}{r^2} \right) + \frac{\sigma_1^{02} - \sigma_2^{02}}{2} \frac{a^2}{r^2} \left( 1 + \frac{3a^2}{r^2} \right) - \frac{(\sigma_1^0 - \sigma_2^0)^2}{4} \left( 1 - \frac{3a^2}{r^2} \right) \left( 1 + \frac{3a^4}{r^4} \right) \right] \right\} \end{aligned}$$

**Appendix B. Derivation of Eq. (8)**

For the case of initial hydrostatic stress  $p$  considered here, the stress components  $\sigma_r^*, \sigma_\theta^*, \tau_{r\theta}^*$  are given by (Kirsch, 1898):

$$\begin{cases} \sigma_r^* = \frac{\sigma_1^0 + \sigma_2^0}{2} \left(1 - \frac{a^2}{r^2}\right) \\ \sigma_\theta^* = \frac{\sigma_1^0 + \sigma_2^0}{2} \left(1 + \frac{a^2}{r^2}\right) \\ \tau_{r\theta}^* = 0 \end{cases} \tag{B.1}$$

Considering the tunnel coordinate system (Fig. 4b) and orthogonal joints, the angle  $\alpha$  between the  $x$  axis and the radius vector  $r$  may be expressed as:

$$\begin{aligned} \cos\alpha &= \frac{-x}{r} = \frac{-x}{\sqrt{x^2 + y^2}} \\ \sin\alpha &= \frac{y}{r} = \frac{y}{\sqrt{x^2 + y^2}} \end{aligned} \tag{B.2}$$

The radial stress after the opening is made  $\sigma_r^*$  acting on trace  $l_{PD}$  and the tangential stress after the excavation is made  $\sigma_\theta^*$  acting on trace  $l_{OP}$  vary at every point  $P$  near the opening, and since we are assuming initial hydrostatic stress  $p$ , the shear stress  $\tau_{r\theta}^*$  must equal to zero, as evident from Eq. (B.1). To find the horizontal force component  $F_{th}$  acting on inclined joint segment  $l_{AB}$  due to radial stress  $\sigma_r^*$ , we consider the angles between  $\sigma_r^*$  and horizontal trace  $l_{PG}$  ( $\alpha$ ) and between  $l_{PD}$  and joint segment  $l_{AB}$  ( $45^\circ - \alpha$ ), and integrate the horizontal differential  $dF_{th}$  ( $=dF_r \cos\alpha$ ) shown in Fig. 4c, over the length of joint segment  $l_{AB}$ :

$$\begin{aligned} F_{th} &= \int_{l_{AB}} dF_{th} = \int_{l_{PD}} dF_r \cos\alpha = \int_{l_{PD}} \sigma_r^* dl_{PD} (\times 1 \text{ m}) \cos\alpha \\ &= \int_{l_{AB}} \sigma_r^* \cos(45^\circ - \alpha) dl_{AB} (\times 1 \text{ m}) \cos\alpha \\ &= \frac{\sqrt{2}}{2} \int_{l_{AB}} \sigma_r^* (\cos\alpha + \sin\alpha) \cos\alpha dl_{AB} (\times 1 \text{ m}) \end{aligned} \tag{B.3}$$

The linear segment  $l_{AB}$  can be expressed as  $y = f(x)$ , where  $f(x)$  has a continuous derivative  $f'(x)$  in the  $x$ - $y$  coordinate system. The length of  $l_{AB}$  is therefore (Anton et al., 2012)

$$\int_A^B dl_{AB} = \int_A^B \sqrt{1 + \left(\frac{dy}{dx}\right)^2} dx \quad (\text{B.4})$$

The distance between point  $P$  and the tunnel center  $O$  is  $r = \sqrt{x^2 + y^2}$  as indicated in Fig. 4b. To find the horizontal force component acting on the analyzed keyblock due to stresses acting on block boundary  $l_{AB}$  in an initially hydrostatic stress field of magnitude  $p$  we substitute into Eq. (B.3)  $\sigma_r^*$  from Eq. (B.1),  $\cos \alpha$  and  $\sin \alpha$  from Eq. (B.2), and the length of  $l_{AB}$  from Eq. (B.4):

$$F_{rh} = \frac{\sqrt{2}(2p)}{4} \int_A^B \frac{-x(y-x)}{x^2 + y^2} \left(1 - \frac{a^2}{x^2 + y^2}\right) \sqrt{1 + \left(\frac{dy}{dx}\right)^2} dx \times 1 \text{ m} \quad (\text{B.5})$$

For the example shown in Fig. 4b, the coordinates of points A and B are A (−3.9950, 0.2004), B (−4.1953, 0), the tunnel radius  $a$  is 4 m, and let us assume an initial hydrostatic stress of  $\sigma_1^0 = \sigma_2^0 = p = 30\text{MPa}$ . In this tunnel coordinate system line  $l_{AB}$  can be expressed as:  $y = x + 4.1953$ . Substituting these parameters into Eq. (B.5) we get the magnitude of the horizontal force component acting on the analyzed keyblock due to radial stress  $\sigma_r^*$  acting on boundary  $l_{AB}$ :

$$\begin{aligned} F_{rh} &= \frac{(30+30) \times 10^6}{2} \int_{-3.9950}^{-4.1953} \frac{-4.1953x}{x^2 + (x+4.1953)^2} \left[1 - \frac{16}{x^2 + (x+4.1953)^2}\right] dx \times 1 \text{ m} \\ &= 1417419(\text{N}) \end{aligned} \quad (\text{B.6})$$

Likewise, the horizontal force component  $F_{\theta h}$  acting on line  $l_{AB}$  from tangential stress  $\sigma_{\theta}^*$  can be calculated by integrating the infinitesimal force  $dF_{\theta h}$  over the block boundary  $l_{AB}$  (Fig. 4c):

$$\begin{aligned} F_{\theta h} &= \int_{l_{AB}} dF_{\theta h} = \int \sigma_{\theta}^* \sin \alpha \cos(45^\circ + \alpha) dl_{AB} \times 1 \text{ m} \\ &= \int_A^B \sqrt{1 + \left(\frac{dy}{dx}\right)^2} \sin \alpha \cos(45^\circ + \alpha) \sigma_{\theta}^* dx \times 1 \text{ m} \\ &= \frac{-\sigma_1^0 + \sigma_2^0}{2} \int_{-3.9950}^{-4.1953} \frac{(x+4.1953)(2x+4.1953)}{x^2 + (x+4.1953)^2} \left[1 + \frac{16}{x^2 + (x+4.1953)^2}\right] dx \times 1 \text{ m} \\ &= 1417365(\text{N}) \end{aligned} \quad (\text{B.7})$$

The two horizontal force components  $F_{rh}$  and  $F_{\theta h}$  contribute to horizontal force  $F_h$  acting on inclined keyblock boundary  $l_{AB}$ . Clearly due to symmetry, the horizontal force components acting on keyblock boundaries  $l_{AB}$  and  $l_{BC}$  must be equal. The vertical force resultants from stresses acting on  $l_{AB}$  and  $l_{BC}$  are counteracted and do not contribute to the horizontal force acting on the keyblock. The analysis presented here clearly shows that the horizontal resultant force acting on the keyblock ( $F_h = F_{rh} + F_{\theta h}$ ) depends on joint orientation ( $\alpha$ ), initial stress ( $p$ ), opening radius ( $a$ ), and keyblock size as scaled by joint spacing along with tunnel diameter.

As discussed qualitatively above, once the tunnel rock is removed the block will open from the boundary joints and will fly at a horizontal trajectory into the tunnel space. Once the keyblock is detached from the rockmass the forces acting on the block will diminish and consequently the block acceleration will drop to zero. The velocity of the block, however, will remain constant as long as it flies in the space of the tunnel (recall that gravity is ignored). With the horizontal force resultant determined analytically (Eqs. (B.6) and (B.7)) we can now find the peak acceleration of the keyblock at the instance it begins to move:

$$a = \frac{F}{m} = \frac{2 \times (F_{rh} + F_{\theta h})}{S_{ejection} \times 1 \text{ m} \times \rho} = \frac{2 \times (1417365 \text{ N} + 1417419 \text{ N})}{0.038 \text{ m}^2 \times 1 \text{ m} \times 2563.8 \text{ kg/m}^3} = 58363 \text{ m/s}^2 \quad (\text{B.8})$$

where the area of the keyblock (Fig. 4b) is  $0.038 \text{ m}^2$ .

## References

- Adoko, A.C., Gokceoglu, C., Wu, L., Zuo, Q.J., 2013. Knowledge-based and data-driven fuzzy modeling for rockburst prediction. *Int. J. Rock Mech. Min. Sci.* 61, 86–95.
- Anton, H., Bivens, I., Davis, S., 2012. *Calculus Single Variable*, tenth ed. John Wiley & Sons, Jefferson, USA.
- Bao, H.R., Hatzor, Y.H., Huang, X., 2012. A new viscous boundary condition in the two-dimensional discontinuous deformation analysis method for wave propagation problems. *Rock Mech. Rock Eng.* 45 (5), 919–928.
- Barton, N., Lien, R., Lunde, J., 1974. Engineering classification of rock masses for the design of tunnel support. *Rock Mech.* 6 (4), 189–236.
- Bieniawski, Z.T., 1976. *Rock Mass Classifications in Rock engineering*. In: Bieniawski Z.T. (Ed.), *Proceedings Symposium on Exploration for rock Engineering* (pp. 97–106). Rotterdam, Netherlands.
- Bieniawski, Z.T., 1973. Engineering classification of jointed rock masses. *Trans. S. A. Inst. Civ. Eng.* 15 (12), 335–344.
- Brady, B.T., Leighton, F.W., 1977. Seismicity anomaly prior to a moderate rockburst: a case study. *Int. J. Rock Mech. Min. Sci. Geomech. Abstr.* 14 (3), 127–132.
- Chen, B.R., Feng, X.T., Li, Q.P., Luo, R.Z., Li, S.J., 2015. Rock burst intensity classification based on the radiated energy with damage intensity at Jinping II hydropower station, China. *Rock Mech. Rock Eng.* 48 (1), 289–303.
- Cook, N.G.W., 1966. *Rock Mechanics Applied to the Study of Rockbursts*. South African Institute of Mining and Metallurgy, Johannesburg.
- Feng, X.T., Chen, B.R., Li, S.J., Zhang, C.Q., Xiao, Y.X., Feng, G.L., Zhou, H., Qiu, S.L., Zhao, Z.N., Yu, Y., Chen, D.F., Ming, H.J., 2012. Studies on the evolution process of rockbursts in deep tunnels. *J. Rock Mech. Geotech. Eng.* 4 (4), 289–295.
- Feng, X.T., Yu, Y., Feng, G.L., Xiao, Y.X., Chen, B.R., Jiang, Q., 2016. Fractal behaviour of the microseismic energy associated with immediate rockbursts in deep, hard rock tunnels. *Tunn. Undergr. Space Technol.* 51, 98–107.
- Feng, X.T., Chen, B.R., Zhang, C.Q., Li, S.J., Wu, S.Y., 2013. *Mechanism, Warning and Dynamic Control of Rockburst Development Processes*. Science Press, Beijing (in Chinese).
- Gong, W.L., Peng, Y.Y., Wang, H., He, M.C., Sousa, L.R., Wang, J., 2014. Fracture angle analysis of rock burst faulting planes based on true-triaxial experiment. *Rock Mech. Rock Eng.* 48 (3), 1017–1039.
- Goodman, R.E., Shi, G.H., 1985. *Block Theory and its Application to Rock Engineering*. Prentice-Hall, New Jersey.
- He, B.G., Zelig, R., Hatzor, Y.H., Feng, X.T., 2016. Rockburst generation in discontinuous rock masses. *Rock Mech. Rock Eng.* 49 (10), 4103–4124.
- He, M.C., Sousa, L.R., Miranda, T., Zhu, G.L., 2015. Rockburst laboratory tests database — application of data mining techniques. *Eng. Geol.* 185, 116–130.
- He, M.C., Xia, H.M., Jia, X.N., Gong, W.L., Zhao, F., Liang, K.Y., 2012. Studies on classification, criteria and control of rockbursts. *J. Rock Mech. Geotech. Eng.* 4 (2), 97–114.
- Hedley, D.G.F., 1992. *Rockburst handbook for Ontario hardrock mines*. CANMET Special Report SP92-1E, ninth ed. Canada Communication Group-Publishing, Ottawa, Canada.
- Hoek, E., Brown, E.T., 1980. *Underground Excavations in Rock*. Institution of Mining & Metallurgy, London.
- Hoek, E., Brown, E.T., 1997. Practical estimates of rock mass strength. *Int. J. Rock Mech. Min. Sci.* 34 (8), 1165–1186.
- Hoek, E., Kaiser, P.K., Bawden, W.F., 1995. *Support of Underground Excavations in Hard Rock*. A.A. Balkema, Rotterdam.
- Hudyma, M.R., Heal, D., Mikula, P., 2003. Seismic monitoring in mines — old technology — new applications. In: *Proceedings of the First Australasian Ground Control in Mining Conference* (pp. 201–218). UNSW school of Mining Engineering, Sydney.
- Kaiser, P.K., Cai, M., 2012. Design of rock support system under rockburst condition. *J. Rock Mech. Geotech. Eng.* 2012 (3), 215–227.
- Kirsch, E.G., 1898. *Die Theorie der Elastizität und die Bedürfnisse der Festigkeitslehre*.

- Zeitschrift Des Vereines Deutscher Ingenieure 42 (28), 797–807.
- Li, S.J., Feng, X.T., Li, Z.H., Chen, B.R., Zhang, C.Q., Zhou, H., 2012. In situ monitoring of rockburst nucleation and evolution in the deeply buried tunnels of Jinping II hydropower station. *Eng. Geol.* 137–138, 85–96.
- Li, S.J., Feng, X.T., Li, Z.H., Chen, B.R., Jiang, Q., Wu, S.Y., Hu, B., Xu, J.S., 2011. In situ experiments on width and evolution characteristics of excavation damaged zone in deeply buried tunnels. *Sci China Technol Sci.* 54 (1 SUPPL.).
- Li, Z.P., Xu, G.L., Dong, J.X., Chu, H.D., Wang, J.S., Chen, C.W., 2017. Geomechanics mechanism and characteristics of surrounding rock mass failure for underground powerhouse under high geostress. *J. Cent. S. Univ. (Sci. Technol.)* 48 (6), 1568–1576 (in Chinese).
- Liu, L.P., Wang, X.G., Zhang, Y.Z., Jia, Z.X., Duan, Q.W., 2011. Tempo-spatial characteristics and influential factors of rockburst: a case study of transportation and drainage tunnels in Jinping II hydropower station. *J. Rock Mech. Geotech. Eng.* 3 (2), 179–185.
- Liu, G.F., Feng, X.T., Feng, G.L., Chen, B.R., Chen, D.F., Duan, S.Q., 2016. A method for dynamic risk assessment and management of rockbursts in drill and blast tunnels. *Rock Mech. Rock Eng.* 49 (8), 3257–3279.
- Martin M.N., 1970. *A Comprehensive Review on Rock Burst* (M.Sc. thesis). Massachusetts Institute of Technology, USA.
- Mazaira, A., Konicek, P., 2015. Intense rockburst impacts in deep underground construction and their prevention. *Can. Geotech. J.* 52 (10), 1426–1439.
- Mendecki, A.J., Lynch, R.A., Malovichko, D.A., 2010. *Routine Micro-Seismic Monitoring in Mines*. In: Australian Earthquake Engineering Society 2010 Conference (pp. 1–33). Perth, Australia.
- Miao, S.J., Cai, M.F., Guo, Q.F., Huang, Z.J., 2016. Rock burst prediction based on in-situ stress and energy accumulation theory. *Int. J. Rock Mech. Min. Sci.* 83 (4), 86–94.
- Milev, A.M., Spottiswoode, S.M., Rorke, A.J., Finnie, G.J., 2001. Seismic monitoring of a simulated rockburst on a wall of an underground tunnel. *J. S. A. Inst. Min. Metall.* 101 (5), 253–260.
- Müller, W., 1991. Numerical simulation of rock bursts. *Min. Sci. Technol.* 12 (1), 27–42.
- Mutke, G., Dubiński, J., Lurka, A., 2015. New criteria to assess seismic and rock burst hazard in coal mines. *Arch. Min. Sci.* 60 (3), 743–760.
- Obert, L., Duvall, W.I., 1967. *Rock Mechanics and the Design of Structures in Rock*. John Wiley & Sons, New York.
- Ortlepp, W.D., Stacey, T.R., 1994. Rockburst mechanisms in tunnels and shafts. *Tunn. Undergr. Space Technol.* 9 (1), 59–65.
- Perras, M.A., Diederichs, M.S., 2016. Predicting excavation damage zone depths in brittle rocks. *J. Rock Mech. Geotechn. Eng.* 8 (1), 60–74.
- Russenes B.F., 1974. *Analysis of Rock Spalling for Tunnels in Steep Valley Sides* (M.Sc. thesis). Norwegian Institute of Technology.
- Sadd, M., 2009. *Elasticity Theory, Applications and Numerics*. second ed. Elsevier Academic Press, Burlington.
- Shi, G.H., 1993. *Block System Modeling by Discontinuous Deformation Analysis*. Computational Mechanics Publication, Southampton UK and Boston, USA.
- Smading, M.S., Roby, J., Willis, D., 2009. *Onsite Assembly and Hard Rock Tunneling at the Jinping-II Hydropower Station Power Tunnel Project*. Society for Mining Metallurgy & Exploration, Las Vegas, pp. 1308–1320.
- Tal, Y., Hatzor, Y.H., Feng, X.T., 2014. An improved numerical manifold method for simulation of sequential excavation in fractured rocks. *Int. J. Rock Mech. Min. Sci.* 65, 116–128.
- TB10003-2005, 2005. *Code for design on tunnel of railway*. The Professional Standards Compilation Group of People's Republic of China, Beijing, China (in Chinese).
- Timoshenko, S.P., Goodier, J.N., 1970. *Theory of Elasticity*, 3rd ed. McGraw-Hill, New York.
- Turchaninov, I.A., Markov, G.A., Gzovsky, M.V., Kazikayev, D.M., Frenze, U.K., Batugin, S.A., Chabdarova, U.I., 1972. State of stress in the upper part of the Earth's crust based on direct measurements in mines and on tectonophysical and seismological studies. *Phys. Earth Planet. Inter.* 6 (4), 229–234.
- Ünal, E., 1996. Modified rock mass classification: M-RMR system. In: Bieniawski, Z. (Ed.), *Milestone in rock engineering: a jubilee collection*. A.A. Balkema, Rotterdam, pp. 203–223.
- Urbanic, T., Feignier, B., Young, R., 1992. Influence of source region properties on scaling relations for  $M < 0$  events. *Pure Appl. Geophys.* 139 (3), 721–739.
- Voinov, K.A., Krakov, A.S., Lomakin, V.S., Khalevin, N.I., 1987. Seismological studies of rock bursts at the Northern Ural bauxite deposits. *Izv. Akad. Nauk SSSR. Fiz. Zemli* 10 (98–104).
- Wang, G.F., Gong, S.Y., Li, Z.L., Dou, L.M., Cai, W., Mao, Y., 2015a. Evolution of stress concentration and energy release before rock bursts: two case studies from Xingan Coal mine, Hegang, China. *Rock Mech. Rock Eng.* 49 (9), 3393–3401.
- Wang, H.J., Liu, D.A., Gong, W.L., Li, L.Y., 2015b. Dynamic analysis of granite rockburst based on the PIV technique. *Int. J. Min. Sci. Technol.* 25 (2), 275–283.
- Wang, J.A., Park, H.D., 2001. Comprehensive prediction of rockburst based on analysis of strain energy in rocks. *Tunn. Undergr. Space Technol.* 16 (1), 49–57.
- Xiao, Y.X., Feng, X.T., Li, S.J., Feng, G.L., Yu, Y., 2016. Rock mass fracturing mechanisms during the evolution process of rockbursts in tunnels. *Int. J. Rock Mech. Min. Sci.* 83, 174–181.
- Zembaty, Z., 2004. Rockburst induced ground motion—a comparative study. *Soil Dyn. Earthq. Eng.* 24 (1), 11–23.
- Zhang, C.Q., Feng, X.T., Zhou, H., Qiu, S.L., Wu, W.P., 2012a. Case histories of four extremely intense rockbursts in deep tunnels. *Rock Mech. Rock Eng.* 45 (3), 275–288.
- Zhang, C.Q., Zhou, H., Feng, X.T., 2011. An index for estimating the stability of brittle surrounding rock mass: FAI and its engineering application. *Rock Mech. Rock Eng.* 44 (4), 401–414.
- Zhang, C.Q., Feng, X.T., Zhou, H., Qiu, S.L., Wu, W.P., 2012b. A top pilot tunnel pre-conditioning method for the prevention of extremely intense rockbursts in deep tunnels excavated by TBMs. *Rock Mech. Rock Eng.* 45 (3), 288–309.
- Zhang, C.Q., Feng, X.T., Zhou, H., Qiu, S.L., Yang, Y.S., 2014. Rock mass damage induced by rockbursts occurring on tunnel floors: a case study of two tunnels at the Jinping II Hydropower Station. *Environ. Earth Sci.* 71 (1), 441–450.
- Zhao, G.B., Wang, D.Y., Gao, B., Wang, S.J., 2017. Modifying rock burst criteria based on observations in a division tunnel. *Eng. Geol.* 216, 153–160.
- Zhou, H., Meng, F.Z., Zhang, C.Q., Hu, D.W., Yang, F.J., Lu, J.J., 2015. Analysis of rockburst mechanisms induced by structural planes in deep tunnels. *Bull. Eng. Geol. Env.* 74 (4), 1435–1451.